Displays 85 (2024) 102835

Contents lists available at ScienceDirect

Displays

journal homepage: www.elsevier.com/locate/displa

Review

Statistical techniques for digital pre-processing of computed tomography medical images: A current review☆

Oscar Valbuena Prada [a,*], Miguel Ángel Vera [a], Guillermo Ramirez [b], Ricardo Barrientos Rojel [c], David Mojica Maldonado [d]

[a] Universidad Simón Bolívar, Departamento de Ciencias Básicas, Sociales y Humanas, San José de Cúcuta, 540000-19, Colombia
[b] Universidad Central de Venezuela, Departamento de Estadística y Actuariado, Caracas, 1050, Venezuela
[c] Universidad Católica del Maule, Facultad de Ciencias de la Ingeniería, Talca, 3460000, Chile
[d] Universidad Simón Bolívar, Departamento de TI, San José de Cúcuta, 540000-19, Colombia

ARTICLE INFO

Keywords:
Statistical techniques
Metrics
Pre-processing of medical images
Multilayer computed tomography
Noise
Artifacts

ABSTRACT

Digital pre-processing is a vital stage in the processing of the information contained in multilayer computed tomography images. The purpose of digital pre-processing is the minimization of the effect of image imperfections, which are associated with the noise and artifacts that affect the quality of the images during acquisition, storage, and/or transmission processes. Likewise, there is a wide variety of techniques in specialized literature that address the problem of imperfections, noise, and artifacts present in images. In this study, a comprehensive review of specialized literature on statistical techniques used in the pre-processing of digital images was conducted. The review summarizes updated information from 56 studies conducted over the last 5 years (2018–2022) on the main statistical techniques used for the digital processing of medical images obtained under different modalities, with a special focus on computed tomography. Additionally, the most often used statistical metrics for measuring the performance of pre-processing techniques in the field of medical imaging are described. The most often used pre-processing techniques in the field of medical imaging were found to be statistical filters based on median, neural networks, Gaussian filters based on deep learning, mean, and machine learning applied to multilayer computed tomography images and magnetic resonance images of the brain, abdomen, lungs, and heart, among other organs of the body.

Contents

☆ This paper was recommended for publication by Prof. Guangtao Zhai.

* Corresponding author.
E-mail address: valbuenaosc@gmail.com (O.V. Prada).

https://doi.org/10.1016/j.displa.2024.102835
Received 1 May 2024; Received in revised form 4 September 2024; Accepted 6 September 2024
Available online 14 September 2024

1. Introduction

In the last decade, research on medical imaging has progressed significantly, as evidenced by technological advancements in image acquisition equipment as well as the development and implementation of pre-processing techniques to reduce imperfections, noise, and artifacts in images. This has allowed us to address problems that require the use of software and equipment with large data storage and processing capacity through the incorporation of models and statistical techniques for the pre-processing and digital analysis of information contained in medical images. There has been a great scientific interest in the development of new and better pre-processing algorithms that reduce image imperfections. These algorithms are based on first- and second-order statistical principles applied to the context of medical imaging, mainly because they provide good performance in terms of improving the quality of the information present in images while also having a low cost in terms of computing time. Additionally, unlike other more complex techniques, these algorithms do not demand a robust and specialized computing infrastructure, not only because of the mathematical models that must be implemented but also because they require a larger infrastructure. However, from the perspective of improving the quality of information, these algorithms offer quite similar results. On the other hand, it is worth noting that there is no image processing technique

that allows for the pre-processing of a set of images acquired using different medical imaging modalities and of images of different parts and organs of the human body. Although several studies on image pre-processing have been reported in specialized literature, they vary based on the image acquisition modality and the type of imperfections present, which are associated with both equipment operating factors, such as the energy and dose used to irradiate the patient, and external factors related to the patient's characteristics, such as the voluntary and involuntary movement of the body and internal organs during image acquisition. Nevertheless, techniques based on statistical principles, such as mean, median, and maximum and minimum, have been found to be commonly used in most studies on medical image processing. Moreover, it is important to stress the importance of the process of evaluating pre-processing algorithms when identifying the extent to which they improve the quality of the image information while reducing noise and artifacts present in the images. A significant number of statistical metrics have been reported in specialized literature that offer information regarding image quality in terms of brightness, sharpness, and contrast, such that improvements in the quality of the information provided by the pre-processing algorithms can be quantified. The different types of metrics help quantify such improvements, thereby allowing the measurement of the efficiency and robustness of different pre-processing algorithms. To date, the main noises and artifacts that affect images have been characterized based on the image acquisition modality; however, a threshold of imperfections remain that cannot be directly quantified from real images. In this regard, synthetic images called Phantom are used, which are essentially an uncontaminated image version from which an image is generated with the intentional addition of a type of noise or known artifact. This method is widely used to determine whether an algorithm is indeed reducing imperfections and substantially contributing to the improvement of the image. This is achieved by comparing the uncontaminated image with its filtered version obtained using pre-processing algorithms. However, an image version without imperfections cannot be obtained in real images; therefore, tests are usually conducted initially using synthetic images. Nevertheless, there is an array of metrics that act directly on the characteristics of the filtered image and do not require comparison between images to quantify improvements in the quality of the information. This review describes the main medical image pre-processing techniques used under different modalities and presents an array of metrics used to quantify the efficiency of pre-processing algorithms.

In conducting this comprehensive review of statistical techniques for the pre-processing of medical images, a meticulous approach was employed to ensure the inclusion of only the most relevant and rigorous studies. A set of stringent criteria was established to guide the selection process, thereby ensuring the currency, focus, and quality of the research examined. The review was confined to studies published within the recent five-year period from 2018 to 2022, maintaining currency with the latest advancements in the field. The focus was narrowed to research specifically targeting statistical techniques applied to medical image pre-processing, with a particular emphasis on computed tomography (CT) due to its clinical significance. In terms of imaging modalities, the review encompassed a broad range, including CT, magnetic resonance imaging (MRI), X-ray, and ultrasound (US), to capture the diversity of applications across different medical imaging technologies. Crucially, the studies included were required to report on the performance metrics used to evaluate the effectiveness of the pre-processing techniques, providing a quantitative basis for assessing the quality of the image enhancement achieved. The review was further limited to peer-reviewed articles from reputable journals and conferences, ensuring that the studies met the highest standards of academic rigor and transparency. Conversely, studies were disqualified if they were not centered on medical image processing or if they lacked the necessary detail on the techniques and metrics, as this would undermine the integrity and utility of the review. This methodical approach to study selection ensured that the review was both comprehensive and discerning, providing a robust foundation for the analysis and conclusions drawn.

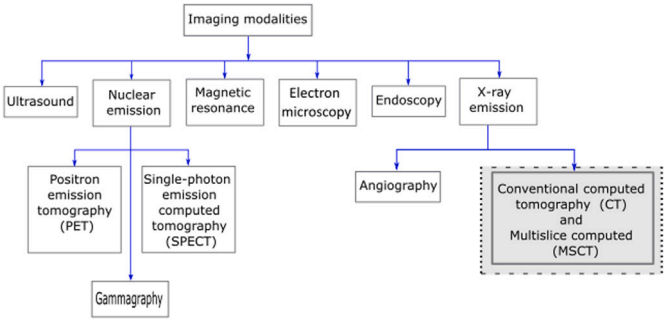

Fig. 1. Comparative overview of imaging modalities for medical diagnosis.

2. Methodology

To enhance the coherence and logical flow of the results section, the findings have been grouped into three major categories: Medical Imaging Modalities, Statistical Techniques and Evaluation Metrics.

2.1. Medical imaging modalities

The results are further organized based on the medical imaging modalities CT, MRI, X- ray, and US. Each modality is discussed concerning the pre-processing techniques that are most effective in addressing specific artifacts and noise issues, with examples from the literature to support these findings.

Advances in artificial intelligence and its applications in the processing and interpretation of digital information have allowed doctors to have clinical support tools that favor a better interpretation of information, thus enabling better diagnosis in the preventive, operative, and postoperative stages [1]. It is also important to note that there are different modalities in medical image acquisition, which are defined according to the energy used to irradiate the patient [2]. Fig. 1, shows the different modalities of medical image acquisition, among which MSCT stands out.

2.1.1. Ultrasound (US)

Medical images obtained using US are derived from the mechanical energy that propagates through tissues and is reflected at different frequencies owing to the differences in tissue density. US employs nonionizing radiation to produce a single-slice tomography image, with US scan being the imaging modality that uses this type of noninvasive energy [3].

2.1.2. Nuclear imaging

Nuclear imaging is characterized by the use of radioactive biomarkers (radioisotopes) to trace the metabolic pathways of an organism. It is based on the detection and quantification of the gamma rays of biomarkers as they move through the body [4]. This technique uses energy that may cause injury to different organs of the body, which is why biomarker dosimetry protocols are crucial. Nuclear emission imaging is subdivided into positron emission tomography *(PET)*, which considers the traces emitted by positrons as reference to generate images by tomographic reconstruction, and single-photon emission computed tomography *(SPECT)*, which involves emission and scattering phenomena derived from the photoelectric and Compton effects. Photons are detected by a set of two-dimensional *2-D* sensors, and the tomographic three-dimensional *3-D* image is obtained through a reconstruction process similar to that of *PET* [5].

2.1.3. Magnetic resonance imaging (MRI)

Images under this modality are obtained by irradiating the matter that has previously been exposed to an electromagnetic field with

pulses of radiofrequency waves. When interrupting the radiofrequency pulses, energy is released, and radio signals are emitted to be subsequently analyzed using a computer that transforms information into images [6]. This modality provides morphological and functional images with an ample variety of contrasts in soft tissues and good spatial resolution.

2.1.4. Electron microscopy

Electron microscopy is a widely used digital image processing and analysis modality intended to characterize, diagnose, predict, classify, and extract information from tissue or fluid with the aim of differentiating normal from malignant cells. Two modalities are identified based on their resolution power: transmission electron microscopy, which generates thin-section *2-D* images, and scanning electron microscopy, which generates *3-D* images [7].

2.1.5. Endoscopy

This medical imaging modality has advanced significantly from its inception in the 1960s with the introduction of gastrointestinal endoscopy to the incorporation of new technologies today, such as autofluorescence and laser endomicroscopy, which use a part of the spectral band width, it generally corresponds to the standard *RGB* as a result of optical or digital filtering. Images are selected and assigned to one of the *RGB* colors to display an enhanced color composite image in real time [8].

2.1.6. X-ray emission angiography

It is a medical *3-D* tomography modality that involves the emission of *X-rays*. The region of interest is exposed to low doses of radiation according to the density distribution of the tissue. Detection systems interpret the signal information and convert it into digital images [9]. Angiography has been widely used in studies on the cardiovascular system, since it enables the study of veins, arteries, vessels, and cardiac cavities, leading to the development of angiocardiography [10].

2.1.7. Computed tomography (CT)

CT images are obtained by passing a beam of X-rays through the organ of interest. These *X-rays* are emitted by a tube that rotates around the patient, and the attenuation is measured using detectors throughout the trajectory. The attenuation coefficient at each point of the scanned body section is calculated using reconstruction methods [11]. Relative attenuation values are expressed in Hounsfield Units and are represented as a grayscale image [12].

2.1.8. Multislice computed tomography (MSCT)

In this review, special interest is placed on MSCT, an imaging modality that is a variant of CT [13]. MSCT images are acquired through X-ray emission. The output images are stored in a standard format called Digital Imaging and Communications in Medicine, which contains information relative to the identification of the patient and to the characteristics of the tomograph as well as information on images that are the subject of study [14].

Unlike conventional CT, MSCT is based on simultaneous acquisition through a helical or spiral system of more than one tomographic plane and is closely related to the introduction of multidetector acquisition systems for complete human body organ 3D imaging [15]. There are two types of detection systems that enable the simultaneous recording of four tomographic slices: (a) GE Medical Systems, which have an array of 16 individual detectors (1.25-mm-wide each) [16], and (b) Adaptive array detectors, which consist of 8 detectors of 4 different thicknesses (1, 1.5, 2.5, and 5 mm). The thickness of each slice is determined by adjusting the collimator focus and the configuration of the detector arrays. Likewise, images obtained under this modality present noise [17] and artifacts [18] owing to photon emission and the characteristics of the tomography equipment [19]. The Table 1, shows a comparison of the advantages and disadvantages of MSCT.

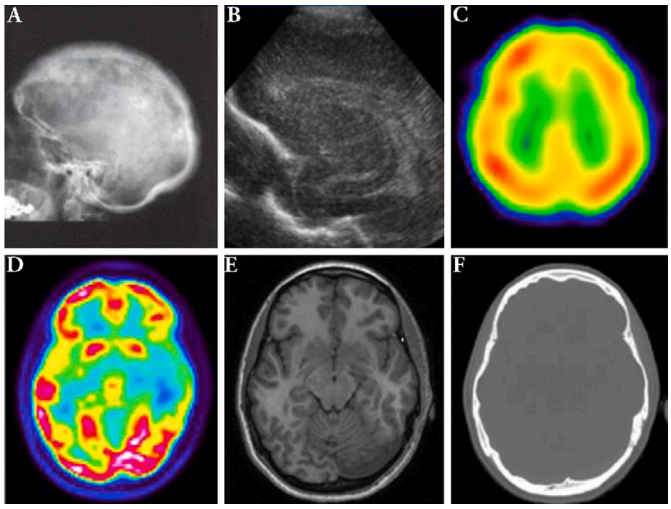

Fig. 2. Multimodal imaging of the human brain: a comparative visual analysis.

In highly specialized procedures, the clinician usually relies on more than one imaging modality for the diagnosis of complex pathologies. These modalities complement each other to help the physician issue a more accurate diagnosis. A set of digital images obtained using different modalities [20], is presented below Fig. 2.

MSCT images are acquired through *X-ray* emission. During this process, random intensities of a grainy appearance appear because of the photon emission and the characteristics of the tomograph, which adds noise and artifacts [17,21].

Noise present in MSCT images: Noise can be interpreted as the random variation of a signal that contaminates the information present in an image, which directly affects its quality [17]. Noise has the following characteristics:

- Noise produced by photon emission is known as quantum noise. Because its generation follows a probability distribution function *(pdf)* of Poisson, it is called Poisson or Poissonian noise and is expressed by Eq. (1).

$$P(n) = \frac{\lambda^n}{n!} exp(-\lambda), \tag{1}$$

  where $P(n)$ denotes the probability of n occurrences of an event and λ denotes the expected value of the *pdf*.
- Poisson noise is a nonadditive noise and is characterized for being dependent on the intensity of each voxel in the image. Higher intensity voxels present a higher statistical probability of being affected by Poissonian noise [22]. This type of noise can be stimulated by creating synthetic data known as numerical phantoms. Fig. 3, shows a pair of synthetic images that illustrate the absence and presence of Poisson noise [23].
- There is a lower probability of finding additive Gaussian white noise in some *MSCT* images.

Artifacts present in MSCT images: In addition to noise, *MSCT* images present artifacts that greatly affect image quality. In *CT* images, the term artifact is attributed to a systematic discrepancy between the Hounsfield values of the images obtained after tomographic reconstruction and the true values for the attenuation coefficients of the objects present in the real image [24].

In *MSCT* images, the most common artifacts are stair-step artifacts and streak or band artifacts. The causes for their occurrence are diverse. Particularly, the streak artifact can be generated by changes in the energy spectrum of the X-rays when X-rays pass through structures containing bone or contrast media [25]. On the other hand, the stair-step artifact may occur as a result of images overlapping during the

Table 1
Advantages and limitations of multilayer spiral computed tomography (MSCT) in medical imaging.

Advantages	Disadvantages
Improves temporal resolution: it decreases artifacts related to the voluntary and involuntary movements of the patient	Radiation exposure, which is highly harmful if several scans are performed
Improvement in the Z-axis spatial resolution: it shows thinner sections while reducing artifacts in the volume and increasing diagnostic accuracy	Movement of the source-detector system: it performs a sweep or translation through the patient
Increase in the concentration of intravenous contrast media: contrast media can be administered faster, thus improving visualization	It is not recommended in pregnant women, since there are potential risks for the developing fetus
Noise reduction: high current values reduce noise in the image	It is not recommended in children because of the risk of developing cancer

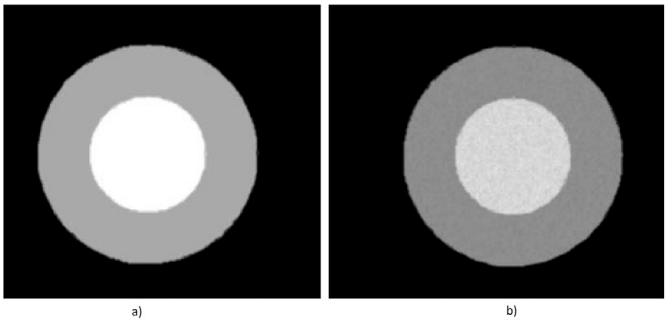

Fig. 3. Synthetic images demonstrating the impact of Poisson noise in medical imaging.

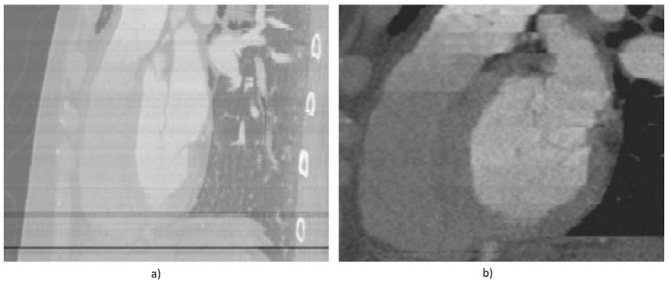

Fig. 4. Axial cardiac images illustrating streak and stair-step artifacts.

reconstruction process or wrong selection of the electrocardiogram triggering phase [18].

This type of artifact impacts geometric characteristics (diameter, surface, or volume), especially those of smaller structures as shown in the Fig. 4 [26].

2.2. Statistical techniques

Medical images obtained through any of the imaging modalities add noise and artifacts that affect the quality of the information in the image [27]. These imperfections hinder their subsequent processing for the segmentation and detection of regions of interest, thereby affecting their interpretation and diagnosis by a clinical expert during decision-making.

The choice of a particular technique can be biased by various factors, such as noise, artifacts, and distortions associated with the modality of image acquisition, as well as adjustment and intonation of the optimal parameters of each of the filtering techniques that will be considered during the pre-processing stage. The intonation and achievement of optimal values for parameters (kernel weights, radios, deviation, and masks or neighborhoods, among others) associated with filtering techniques is essential for assessing and identifying the most efficient and robust filtering technique to increase the image quality, thus constituting a critical factor in the image post-processing and segmentation stages.

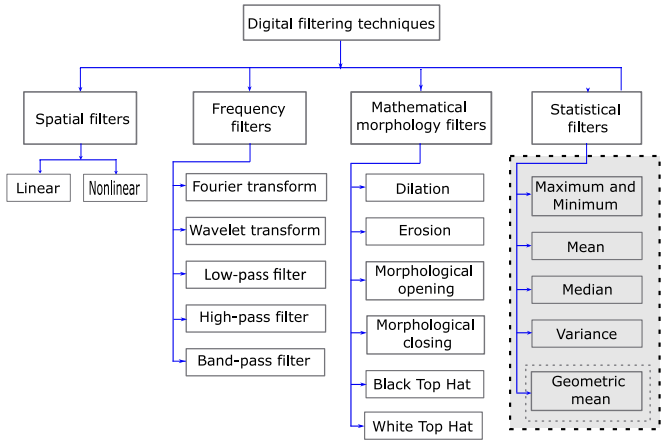

Fig. 5. Digital filtering techniques commonly used in medical image preprocessing.

The main digital filtering techniques commonly used in the preprocessing of medical CT images are summarized in a general way in Fig. 5. Statistical filters are highlighted and will be addressed in a comprehensive manner, identifying the principles of operation, advantages, disadvantages and specific applications in the preprocessing of medical images and will be the subject of study in future research [28]. This includes mean, median, Gaussian filters and other traditional statistical approaches.

2.2.1. Median filter

It is widely used to reduce the noise present in the images and considers the intensity values of the neighbors of the element under study. The median of the array is determined through an array of vectors and the center pixel value is replaced by the value of the neighborhood median [27], according to Eq. (2).

$$g(x,y) = median\{f(s,t)\}, \quad (2)$$

where $(s,t)\ \epsilon\ \ w$, and w denotes a window with a size $(m\ x\ n)$.

2.2.2. Weighted median filter

This filtering technique preserves sharp edges and attenuates the noise present in images. The information of the pixels or voxels adjacent to the pixel or voxel under study is weighted through weights (coefficients) and the gray-level values are repeated as many times as indicated by predefined weighting masks, replacing the values of the neighborhood by the value of the median at the position of each voxel [29].

2.2.3. Permuted median filter

This filtering technique enables the adjustment of weights of the gray levels of the voxels based on the order of the gray levels present in the observation window [30,31].

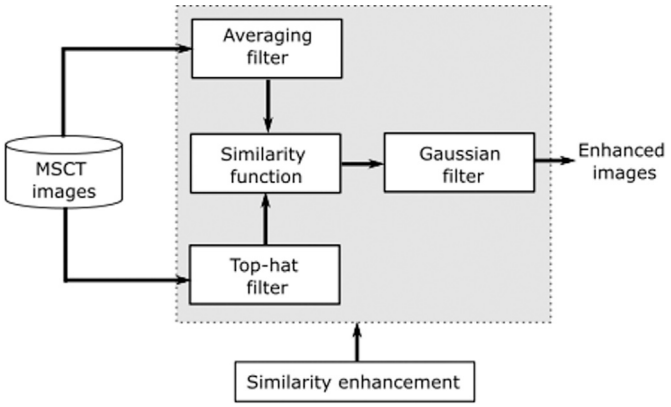

Fig. 6. Enhancing similarity in medical images: a general schematic approach.

2.2.4. Geometric mean filter

This is a variant of the mean filter and represents the geometric average of an array of observations. It is less sensitive to the occurrence of extreme or anomalous observations than the arithmetic mean and is highly efficient in reducing Gaussian noise. For ungrouped data, the geometric mean is expressed using Eq. (3).

$$X_G = \sqrt[n]{\prod_{i=1}^{n} x_i} = \sqrt[n]{x_1 \cdot x_2 \cdot x_3 \dots x_n}, \tag{3}$$

where x_i, is each data; in the case of medical images, it is the statistics associated with the gray level.

2.2.5. Filters based on nonlocal arithmetic means

This is a pre-processing technique for removing noise and preserving detail in digital images. The rationale behind it is that several pixels or voxels present a gray level of an intensity level very similar to that of other elements, regardless of their location in the image [32]. In practice, the value to be modified is replaced by the average of the gray level of the pixels or voxels of those elements bounded in an arbitrary neighborhood. The new intensity of x_i, denoted by $NLM(I(x_i))$, is calculated based on the weighted average of all the gray levels of the elements (x_j) from image I, as indicated in Eq. (4).

$$NLM(I(x_i)) = \sum w(x_i, x_j) I(x_j), \tag{4}$$

For a better understanding of the variants of NLM, see [33].

2.2.6. Similarity enhancement filtering

This is a spatial filtering technique that is widely used in the pre-processing of MSCT images. It operates based on attributes present in images to establish the similarities of two pre-processed versions of an original image. These smoothed versions are obtained through the application of a set of filters, as shown in Fig. 6. On the one hand, the edges of the objects present in one of the versions are highlighted through the use of morphological filters, while on the other hand, they reduce the noise and enhancement the internal information to the edges of the other version by applying a similarity function [34–36]

For its application, the following steps should be considered:

1. Generation of a smoothed output image (Ip) by applying an averaging filter.
   Averaging filter. This filter is used to attenuate the random noise present in medical images. The filter replaces the gray level of the element under study I(x) of an input image with the average gray-level Âμ from the current element's variable radio neighborhood provided that the condition expressed in Eq. (5) is true [37]:

   $$|I(x) - \mu| > \varepsilon. \tag{5}$$

   A threshold (ε).is required for its initialization.
2. Generation of an output black top hat (I_{bTh}) image or an (I_{wTh}) image aimed at enhancing the edges of the objects present in images, replacing the original image I by a smoothed one using a multiscale Gaussian filter (I_{Gme}).
   Black top hat. It is a variant of the top-hat filter that detects intensity variations considering a structuring element and morphological operators [38]. It is called black because the application of this filter tends to darken the input image. The mathematical model of this filter is obtained using Eq. (6) [39].

   $$I_{bTh} = [(I \oplus B) \ominus B] - I, \tag{6}$$

   White top hat. It is called white because the application of this filter tends towards gray levels of greater value present in the input image. The mathematical model of this filter is obtained using Eq. (7) [39].

   $$I_{wTh} = I - [(I \ominus B) \oplus B], \tag{7}$$

Obtention of a similarity picture (I_S), the input of which corresponds to that of the two smoothed versions previously obtained and is denoted as I_{bTh} and I_p, using Eq. (8) [40].

$$I_S = \sum_{l=1}^{n} \left[(a_0 - a_l)^2 + (a_0 - b_l)^2 + (b_0 - a_l)^2\right], \tag{8}$$

where a_l y b_l (with $l = 1, 2, \dots, 6$) are the gray levels of the six neighbors of a_0 and b_0 respectively, n is the number of direct neighbors of such central elements, and a_0 and b_0 are the intensities of the central elements of a neighborhood of arbitrary shape considered on I_{bTh} and I_p, respectively. For a better understanding of the mathematical models, see [35,40].
Finally, a smoothed similarity image is obtained I_{Sg}, through the application of a Gaussian filter to reduce the effect of the top-hat filter [41,42].

Gaussian filter. This is used to attenuate the noise present in medical images. It operates using a discrete Gaussian distribution, which can be expressed by a mask or Gaussian kernel of an arbitrary size [43]. In a *3-D*, image, the scalars comprising the referred kernel can be obtained according to Eq. (9).

$$G(i,j,k) = \frac{1}{\left(\sqrt{2\pi}\right)^3 \sigma_i \sigma_j \sigma_k} e^{-\left(\frac{i^2}{2\sigma_i^2} + \frac{j^2}{2\sigma_j^2} + \frac{k^2}{2\sigma_k^2}\right)}, \tag{9}$$

where $0 \le i, j, k \le (n-1)$, n is the size of the Gaussian kernel, σ_i, σ_j and σ_k are the standard deviations for each spatial dimension. The parameters of this filter are the standard deviation of each of the spatial dimensions, and the radius **r**that defines the size **n** of the mask is given by Eq. (10).

$$n = 2r + 1, \tag{10}$$

where r is an arbitrary scalar.

2.2.7. Variance filter

This is a filter for the detection of blurred or low-contrast edges. This filter is sensitive to changes in the parameter defining the window size in the case of images containing few details but presenting objects with significantly blurred edges. Larger filter windows provide better results. Conversely, images with few details yield better results with smaller windows [44].

$$\sigma^2 = \frac{1}{n} \sum_{i=1}^{W_D^2} \left(u_i - \bar{u}\right)^2, \tag{11}$$

where W_D is the window size and $\bar{u}$ is the mean of u_i and obtained using Eq. (12).

$$\bar{u} = \frac{1}{n} \sum_{i=1}^{W_D^2} u_i \tag{12}$$

2.2.8. Maximum filtering

This is a nonlinear spatial filtering technique based on the ordering of pixels contained in a region, which operates based on the gray-level values in the neighborhood of each point of an image. Once the gray-level values of a neighborhood to a point are sorted, the largest gray-level value is replaced at the position of the central value [28]. This technique is truly useful for removing pepper noise, although it tends to lighten up the image.

2.2.9. Minimum filterings

Unlike maximum filtering, once the gray-level values are ordered, the lowest gray-level value is selected and replaced at the center value position. This technique is truly useful for removing salt noise, although it tends to darken the image.

2.2.10. Filter based on mathematical morphology

This is a nonlinear spatial filtering technique, which operates based on binary images in a gray or color scale by implementing a set of morphological filters based on dilation and erosion operators [41].

- The dilation ($\oplus$) of a image *2-D (I)* using a structuring element (B) is modeled using Eq. (13) [39,45].

$$(I \oplus B)(x,y) = \max_{(s,t) \in B}[I(x-s, y-t) + B(s,t)], \tag{13}$$

  where $m\tilde{A}_i x$ denotes the maximum gray level contained in B.
- The erosion ($\ominus$) of a image *2-D (I)* using a structuring element (B) is modeled using Eq. (14) [39,45].

$$(I \ominus B)(x,y) = \min_{(s,t) \in B}[I(x+s, y+t) - B(s,t)], \tag{14}$$

  where min denotes the minimum gray level contained in B.

In practice, the input image is traversed via a structuring element or window of an arbitrary size, replacing the gray level of each of the image elements by the maximum or minimum gray level contained in the said window, depending on whether the operator is dilation or erosion, following Eqs. (23) and (24). Other morphological filtering techniques that are derived from the combination of the dilation and erosion operators are:

- Morphological closing ($\bullet$), results from applying the erosion operator ($\ominus$) to an input image (I) that has been processed with the dilation operator ($\oplus$). Eq. (15) mathematically models the closing [41].

$$I \bullet B = (I \oplus B) \ominus B, \tag{15}$$

  where B is the structuring element.
- Morphological opening ($\circ$), results from applying the dilation operator to an eroded image to soften the edges and suppress small islands between elements of the image [41]. The opening is modeled using Eq. (16).

$$I \circ B = (I \ominus B) \oplus B, \tag{16}$$

- Black top hat and white top hat filters are also filters based on mathematical morphology, which are obtained with the Eqs. (6) and (7) respectively.

2.2.11. Filter based on the canny operator

This is applied to digital images to detect all of the edges or contours present in an image, considering the abrupt changes in the gray levels of the pixels that comprise the image edges [46–48]. This technique is implemented via the following steps:

1. Reduction of the noise present in the image to be processed.
2. Calculation of the image gradient.
3. Non-maximum suppression to reduce the width of the pixel edges and estimate the direction that best approximates the direction of the gradient.
4. Application of the threshold hysteresis function to eliminate the bifurcations of the segments that join at a point, which requires pre-processing the image with a median filter.

2.3. Evaluation metrics

This subsection categorizes the evaluation metrics used to assess the effectiveness of the pre-processing techniques. Key metrics discussed include PSNR, MSE, SSIM, and others, with a focus on their applicability to different types of image degradation and their role in providing a comprehensive assessment of image quality.

2.3.1. Contrast

The contrast metric is an indicator of the relative difference in the intensity of the gray levels of an image. A high contrast value allows for greater differentiation [49].

$$Contraste = \sum_i \sum_j (i,j)^2 P(i,j) \tag{17}$$

where i and j are different gray levels of the image, and P is the number of the i and j gray level counts.

2.3.2. Entropy

This stipulates the level of uncertainty in the values of the pre-processed image. It measures the spread of the histogram and averages the amount of information to encode the image values. Better image details indicate a higher entropy value [50].

$$Entropia = -\sum_i \sum_j P(i,j) log P(i,j) \tag{18}$$

where $P(i,j)$ is the intensity probability and P is the total number of intensities.

2.3.3. Mean absolute error (MAE)

This estimates the average of the absolute difference per pixel between the reference image and the filtered image [49].

$$MAE = \frac{1}{MN} \sum_{i=0}^{M-1} \sum_{j=0}^{N-1} \left| I_o(i,j) - I_e(i,j) \right|, \tag{19}$$

where MN is the size of the image, I_0 is the original image, and I_e is the filtered image. High values indicate less similarity between the images compared.

2.3.4. Mean square error (MSE)

This calculates the power of the difference in distortion between the reference image and the filtered image. This metric has a low computational cost [51].

$$MSE = \frac{1}{MN} \sum_{i=0}^{M-1} \sum_{j=0}^{N-1} \left(I_o(i,j) - I_e(i,j) \right)^2. \tag{20}$$

where MN represents the total number of pixels in the image.

2.3.5. Peak signal-to-noise ratio (PSNR)

This is the ratio between the maximum possible power of the image and the noise power affecting the quality of its representation. For more information on the model, see [49].

$$PSNR = 10 \log_{10} \left(\frac{MAX_I}{\sqrt{MSE}} \right), \tag{21}$$

where MSE is the mean square error. Eq. (21) can be expressed as follows:

$$PSNR = 10 \log_{10} \left[\frac{(L-1)^2}{\sqrt{MSE}} \right], \tag{22}$$

where $(L-1)$ represents the maximum intensity of the image.

2.3.6. Enhancement measurement estimation (EME)

This determines the largest change in the magnitude of pixel intensities in a specific block of the image. The values obtained are averaged to evaluate the total contrast of the image [49].

$$EME(e) = \frac{1}{k_1 k_2} \sum_{m=1}^{k_1} \sum_{l=1}^{k_2} 20 \ln \left(\frac{I_{max}^{m,l}}{I_{min}^{m,l}} \right), \tag{23}$$

where I is the filtered image, which is divided into blocks of size $k_1 k_2$, I_{max} and I_{min} are the maximum and minimum intensity values in each I block.

2.3.7. Measure of enhancement by entropy (EMEE)

This determines the distribution of gray levels (contrast) in an image, using an entropy function, which increases with an increase in the gray-level number [52].

$$EMEE(e) = \frac{1}{k_1 k_2} \sum_{m=1}^{k_1} \sum_{l=1}^{k_2} \alpha \left(\frac{I_{max}^{m,l}}{I_{min}^{m,l}} \right)^{\alpha} ln \left(\frac{I_{max}^{m,l}}{I_{min}^{m,l}} \right), \tag{24}$$

where α is the scaling constant for each block, with a range between 0 and 1.

2.3.8. Logarithmic michelson contrast measure (AME)

This is very useful for images that do not present texture randomness and have small regions of uniform intensity values [53].

$$AME(e) = -\frac{1}{k_1 k_2} \sum_{m=1}^{k_1} \sum_{l=1}^{k_2} 20 \; ln \left(\frac{I_{max}^{m,l} - I_{min}^{m,l}}{I_{max}^{m,l} + I_{min}^{m,l}} \right), \tag{25}$$

2.3.9. Logarithmic michelson contrast measure by entropy (AMEE)

This refers to the entropy of the Michelson contrast, scaled and averaged over the entire image. AMEE is suitable for images with excessive texture randomness [49].

$$AMEE(e) = -\frac{1}{k_1 k_2} \sum_{m=1}^{k_1} \sum_{l=1}^{k_2} \alpha \left(\frac{I_{max}^{m,l} - I_{min}^{m,l}}{I_{max}^{m,l} + I_{min}^{m,l}} \right)^{\alpha} ln \left(\frac{I_{max}^{m,l} - I_{min}^{m,l}}{I_{max}^{m,l} + I_{min}^{m,l}} \right), \tag{26}$$

2.3.10. Absolute mean brightness error (AMBE)

This quantifies performance in preserving image brightness. A lower AMBE indicates that the brightness is better preserved [54].

$$AMBE(r, e) = \left| \mu_r - \mu_e \right| \tag{27}$$

where r refers to the reference image and e refers to the enhanced image.

2.3.11. Root mean square (RMS)

This is defined as the arithmetic mean of squares of a set of observations. RMS is a general method for evaluating the mean value of errors by directly comparing two sets of data. A higher RMS value indicates a larger error.

$$RMS = \frac{1}{\sqrt{n}} \sqrt{\sum_{i=1}^{n} \left(x_{1,i} - x_{2,i} \right)^2} \tag{28}$$

2.3.12. Second-derivative-like measure of enhancement (SDME)

This metric is based on the second derivative and is less sensitive to noise and edges in images. It provides a quantitative measure of the quality of an image. [55]. SDME works as a local contrast descriptor and is highly sensitive to degradation. The SDME value decreases with an increase in blur or noise variance.

$$SDME(e) = -\frac{1}{k_1 k_2} \sum_{m=1}^{k_1} \sum_{l=1}^{k_2} 20 ln \left| \left(\frac{I_{max}^{m,l} - 2I_{cen}^{m,l} + I_{min}^{m,l}}{I_{max}^{m,l} + 2I_{cen}^{m,l} + I_{min}^{m,l}} \right) \right|, \tag{29}$$

where $I_{cen}^{m,l}$, is the intensity value of the central pixel of each block.

Table 2
Confusion matrix: a tool for assessing classification accuracy in image analysis.

		Predictive Class	
		Positive	Negative
Real class	Positive	TP	FP
	Negative	FN	TN

2.3.13. Metrics based on a confusion matrix

These metrics are based on spatial overlap and statistical classification to evaluate the performance of a pre-processing or segmentation algorithm using supervised learning.

Based on Table 2, the following four basic cardinalities are defined for the fuzzy type:

- True positives (TP). This model correctly classifies the positive class.

$$TP = \sum_{r=1}^{|X|} min \left(f_t^1 \left(x_p \right), f_g^1 \left(x_p \right) \right), \tag{30}$$

  where functions $f_g^i \left(x_p \right)$ and $f_t^j \left(x_p \right)$ determine the probability of belonging to a given point on the corresponding segment $i \in f_g$ and $j \in f_t$.
- False positives (FP). This model incorrectly classifies the negative class.

$$FP = \sum_{r=1}^{|X|} max \left(f_t^1 \left(x_p \right) - f_g^1 \left(x_p \right), 0 \right), \tag{31}$$

- True negatives (TN). This model correctly classifies the negative class.

$$TN = \sum_{r=1}^{|X|} min \left(f_t^2 \left(x_p \right), f_g^2 \left(x_p \right) \right), \tag{32}$$

- False negatives (FN). This model incorrectly classifies the positive class.

$$FN = \sum_{r=1}^{|X|} max \left(f_t^2 \left(x_p \right) - f_g^2 \left(x_p \right), 0 \right), \tag{33}$$

  where $|X| = TP + FP + TN + FN$, represents the total sum of cases.

Another set of metrics is derived from these four cardinalities to determine the sensitivity, specificity, accuracy, and precision of algorithms [56].

2.3.14. True positive rate (TPR, sensitivity)

This metric provides the rate of classified positive cases out of TPs.

$$TPR = \frac{TP}{TP + FN}, \tag{34}$$

2.3.15. True negative rate (TNR, specificity)

This metric provides the rate of classified negative cases out of TNs.

$$TNR = \frac{TN}{TN + FP}, \tag{35}$$

2.3.16. False negative rate (FNR, 1 - sensitivity)

This metric provides the rate of positive cases that are detected as negative by the test.

$$FNR = \frac{FN}{FN + TP} = 1 - TPR, \tag{36}$$

2.3.17. False positive rate (FPR, 1 - specificity)

This metric provides the rate of negative cases that are detected as positive by the test.

$$FPR = \frac{FP}{FP + TN} = 1 - TNR, \tag{37}$$

2.3.18. Positive predictive value (PPV, precision)

This determines the rate of true positive cases among the positive cases detected by the test.

$$PPV = \frac{TP}{TP + FP}, \tag{38}$$

2.3.19. Precision and sensitivity metric (F_β)

This combines PPV precision and TPR sensitivity using a weighting factor, β which controls the balance between both metrics [57].

$$F_\beta = \frac{\left(\beta^2 + 1\right) \times PPV \times TPR}{\beta^2 \times PPV + TPR}, \tag{39}$$

Should the weighting produce a value of $\beta > 1$, it means that the algorithm has a high precision; if $\beta < 1$, it has a high sensitivity; and when $\beta = 1$, the F_β metric is equal to the F_1 measure.

2.3.20. F_1 Measure

It allows measuring the precision of the classification model. It behaves quite well when there is an unequal distribution of classes.

$$F_1 = \frac{2 \times PPV \times TPR}{PPV + TPR}, \tag{40}$$

2.3.21. Dice coefficient (DICE, sørensen–Dice)

This provides a measure of similarity or overlap between two samples. The expected values for the Dice coefficient are real numbers between 0 and 1: a value close to one indicates high similarity between samples, whereas a value close to zero indicates high dissimilarity [58].

$$DICE = \frac{2\left|S_g \cap S_t\right|}{\left|S_g\right| + \left|S_t\right|} = \frac{2TP}{2TP + FP + FN}, \tag{41}$$

where S_g represents (in the context of medical image processing) the image processed manually by a clinical expert (ground truth) and S_t represents that processed by automatic techniques and algorithms.

2.3.22. Jaccard index (JAC)

The JAC metric, like the Dice coefficient, provides a measure of similarity between two samples [56].

$$JAC = \frac{\left|S_g \cap S_t\right|}{\left|S_g \cup S_t\right|} = \frac{TP}{TP + FP + FN}, \tag{42}$$

2.3.23. Global consistency error (GCE)

This is a measure of error between two segmentations, S_1 and S_2, at the position of a voxel x [59].

$$GCE\left(S_t, S_g\right) = \frac{1}{n} min \left\{ \begin{matrix} \frac{FN(FN+2TP)}{TP+FN} + \frac{FP(FP+2TN)}{TN+FP}, \\ \frac{FP(FP+2TP)}{TP+FP} + \frac{FN(FN+2TN)}{TN+FN} \end{matrix} \right\}, \tag{43}$$

2.3.24. Anderberg coefficient

This is a similarity coefficient, the value of which oscillates between 0 and 1. This measure corresponds to the reduction of the real error using one element to predict the other in both directions [55].

$$Anderberg = \frac{TP}{TP + 2 \cdot (FP + FN)}, \tag{44}$$

2.3.25. Blanque coefficient

This metric considers the TPR with respect to the maximum value of the horizontal and vertical sum of FP and FNs, respectively.

$$Blanque = \frac{TP}{max\left\{(TP + FP), (TP + FN)\right\}}, \tag{45}$$

2.3.26. Kulczynski coefficient

This metric is based on the conditional probability that the characteristic present in one element is also present in the other. This index has a lower bound of 0 and no upper bound.

$$Kuczynski = \frac{1}{2} \cdot \left(\frac{TP}{TP + FP} + \frac{TP}{TP + FN}\right), \tag{46}$$

2.3.27. Ochiai coefficienti

This is a variant of the cosine similarity measure with a range of 0–1.

$$Ochiai = \frac{TP}{\left[(TP + FP) + (TP + FN)\right]^{\frac{1}{2}}}, \tag{47}$$

2.3.28. Simpson's coefficient

This considers the TPR with respect to the minimum value of the horizontal and vertical sum of FPs and FNs, respectively.

$$Simpson = \frac{TP}{min\left\{(TP + FP), (TP + FN)\right\}}, \tag{48}$$

2.3.29. Volumetric similarity (VS)

This is a measure of similarity between the volumes of segments [60].

$$VS = 1 - \frac{|FP - FN|}{2 \times TP + FN + FP}, \tag{49}$$

2.3.30. Rand index (RI)

This is a measure of the similarity between data clusters. It is not based on labels and therefore can be used to evaluate both clusters and classifications [61].

$$RI = \frac{TP + TN}{TP + FP + FN + TN}, \tag{50}$$

2.3.31. Adjusted rand index (ARI)

This uses the expected similarity of all pairwise comparisons between clusters, which are specified by a random model [62].

$$ARI = \frac{\sum_{ij}\binom{m_{ij}}{2} - \sum_i \binom{m_i}{2}\sum_j \binom{m_j}{2} / \binom{n}{2}}{\frac{1}{2}\left[\sum_i \binom{m_i}{2} + \sum_j \binom{m_j}{2}\right] - \sum_i \binom{m_i}{2}\sum_j \binom{m_j}{2} / \binom{n}{2}}, \tag{51}$$

where n is the object count, m_{ij} is the confusion matrix, m_{ij} is the sum over the ith row, and m_j denotes the sum over the jth column. columna.

2.3.32. Mutual information metric (MI)

This is a measure of the information contained in a target image (s_t) with respect to a reference image (s_g) [63].

$$MI(s_g, s_t) = H(s_g) + H(s_t) - H(s_g, s_t), \tag{52}$$

The MI measure, in its normalized form, is provided by Eq. (53).

$$MI(s_g, s_t) = \frac{H(s_g) + H(s_t)}{H(s_g, s_t)}, \tag{53}$$

where $H(s_g)$ and $H(s_t)$ are measures of the variation in the image intensity values (s_g) and (s_t), respectively, and $H(s_g, s_t)$ is the measure of the variation in the image intensity value (s_t) in terms of the image (s_g).

2.3.33. Variation of information metric (VOI)

This measures the amount of information lost or added. It also enables the comparison of cluster partitions [64].

$$VOI(s_g, s_t) = H(s_g) + H(s_t) - 2MI(s_g, s_t), \tag{54}$$

2.3.34. Interclass correlation index (ICC)

This is a probabilistic metric that allows the measurement of the agreement between two or more quantitative assessments. It is used as a measure of consistency between two segmentations [65].

$$ICC(s_g, s_t) = \frac{MS_b - MS_w}{MS_b + (k-1)MS_w}, \tag{55}$$

where MS_b and MS_w are given by Eqs. (56) and (57), respectively.

$$MS_b = \frac{2}{n-1}\sum_x (m(x) - \mu)^2, \tag{56}$$

$$MS_w = \frac{1}{n}\sum_x (f_g(x) - m(x))^2 + (f_t(x) - m(x))^2, \tag{57}$$

where MS_b denotes the mean square between the segmentations of the Ms group, MS_w is the mean square within the Ms segmentations, k is the number of segmentations to be compared, μ is the mean of all the means of the two segmentations, and $m(x)$ is the mean in the x voxel, which is determined using Eq. (58).

$$m(x) = (f_g(x) + f_t(x))/2, \tag{58}$$

2.3.35. Probabilistic distance (PBD)

This is a measure of the distance between fuzzy segmentations [66].

$$PDB(S_g, S_t) = \frac{\sum_x \left| f_g(x) - f_t(x) \right|}{2\sum_x f_g(x) f_t(x)}, \tag{59}$$

2.3.36. Cohen's kappa coefficient (KAP)

This is a statistical measure of the level of agreement between two samples. It adjusts for the chance effect on the proportion of the observed agreement [66].

$$KAP = \frac{f_a - f_c}{N - f_c}, \tag{60}$$

where N is the total number of voxels and f_a and f_c are the frequencies, given by Eqs. (61) and (62), respectively.

$$f_a = TP + TN, \tag{61}$$

$$f_c = \frac{(TN + FN)(TN + FP) + (FP + TP)(FN + TP)}{N}, \tag{62}$$

2.3.37. Area under the curve (AUC)

This is the true positive rate vs false positive rate, as determined using a decision threshold [67].

$$AUC = 1 - \frac{FPR + FNR}{2}, \tag{63}$$

where FPR is the true positive rate and FNR is the false positive rate. By substituting them in Eq. (63), Eq. (64), is obtained.

$$AUC = 1 - \frac{1}{2}\left(\frac{FP}{FP + TN} + \frac{FN}{FN + TP}\right), \tag{64}$$

2.3.38. Hausdorff distance (HD)

This is the maximum distance from one set of points to the closest point in another set of points [68].

$$HD(A, B) = max\left(h(A, B), h(B, A)\right), \tag{65}$$

where $h(A, B)$ is the direct distance of the A set to the B set and $h(B,A)$ is the inverse HD, and they are determined by Eqs. (66) and (67), respectively.

$$h(A, B) = \max_{a\in A} \min_{b\in B} \|a - b\|, \tag{66}$$

$$h(B, A) = \max_{b\in B} \min_{a\in A} \|b - a\|, \tag{67}$$

where $\|\cdot\|$ is the norm; for example, the Euclidean norm or that of the maximum.

2.3.39. Hausdorff distance mean (HDM)

In image processing, when applying the HDM, two main problems occur – the scale and the outliers – which can be resolved by implementing a variant of the HDM [69].

$$AVD(A, B) = max(d(A, B), d(B, A)), \tag{68}$$

where $d(A, B)$ and $d(B, A)$ are determined using Eqs. (69) and (70), respectively.

$$d(A, B) = \frac{1}{|A|}\sum_{a\in A} \min_{b\in B} \|a - b\|, \tag{69}$$

$$d(B, A) = \frac{1}{|B|}\sum_{b\in B} \min_{a\in A} \|b - a\|, \tag{70}$$

2.3.40. Mahalanobis distance (MHD)

This considers the correlation of all the points in the cloud with respect to two reference points, with the interaction between coefficients through the covariance matrix [70].

$$MHD(x, y) = \sqrt{(x - y)^T S^{-1}(x, y)}, \tag{71}$$

where S^{-1} is the inverse of the S covariance matrix from the cloud of points, T denotes the transposed matrix, and (x, y) are at the same point in the cloud.

In image processing, the means of the two clouds of points and the covariance matrix are compared using a variant of *MHD* based on Eq. (72) [71].

$$MHD(x, y) = \sqrt{(\mu_x - \mu_y)^T S^{-1}(\mu_x - \mu_y)}, \tag{72}$$

where μ_x and μ_y are the means of the sets of points, and the covariance matrix S is determined using Eq. (73).

$$S = \frac{n_1 S_1 + n_2 S_2}{n_1 + n_2}, \tag{73}$$

where S_1 and S_2 are the covariance matrices, and n_1 and n_2 are the numbers of voxels in each set.

2.3.41. Tanimoto similarity coefficient

This is a measure of the degree of similarity between two sets. Its value ranges from 0 to 1, where 0 represents maximum dissimilarity and 1 represents maximum similarity [55].

$$Tanimoto = \frac{TP + TN}{TP + 2\times FP + 2\times FN + TN}, \tag{74}$$

2.3.42. Conformity metric

This is the ratio of the number of incorrectly segmented pixels to that of correctly segmented pixels [72].

$$Conformity = 1 - \frac{FP + FN}{TP}, \tag{75}$$

where $TP = FP + FN$, represents the case in which Conformity equals zero, negative values mean that $TP < FP + FN$, and minus infinity occurs when $TP = 0$, a case in which there is no intersection between the segmented and real images.

3. Literature review of digital pre-processing techniques and evaluation metrics used to measure the quality of medical images

Statistical preprocessing techniques are diverse and vary according to the modality of acquisition of medical images, most of them are sets of variants of other techniques. Likewise, filtering techniques vary depending on the objective of the preprocessing, whether to reduce noise and artifacts, extract features or segment regions of interest. On the other hand, preprocessing algorithms need metrics to quantify the improvements in the quality of the information present in the medical images. Based on these three aspects, this paper reviews the current status of the main filtering techniques reported in the specialized

Table 3
Preprocessing techniques and metrics employed in medical imaging studies: a comprehensive listing.

Organ	Reference	Year	Modality	Filters	Metrics
Abdomen	[73]	2022	CT	Mean, Gaussian, median, and minimum filter	MSE, PSNR and SSIM
	[74]	2022	US	Mean, median, Kuan, Lee, Frost, others	PSNR, RMSE, SSI, STM and SSIM
	[75]	2021	CT	Strain artifact reduction technique	Artifact index
	[76]	2020	CT	Median, Gaussian, two-sided filter	SSIM, PSNR
	[77]	2019	CT	Two-sided tridimensional transversal filter	Noise power spectrum, others
	[78]	2019	CT	Gaussian Dynamic Process	Principal components, Hausdorff distance
Brain	[79]	2022	CT	Neural convolutional network	Binary precision, sensitivity, and specificity
	[80]	2021	CT	Filter based on median	PSNR and SSIM
	[81]	2021	SPECT, PET	Deep learning algorithms	Specificity, sensitivity, and variance
	[82]	2021	MRI	Median, high-pass filter	Mean, entropy, correlation
	[83]	2021	MRI	Gaussian filter and histogram equalization	MSE, PSNR and SSIM
	[84]	2021	CT, MRI	Segment graphic filter and sparse representation	Structure metric, entropy, congruence
	[85]	2021	CT	Automatic detection algorithm	Precision, performance
	[86]	2021	CT, MRI, others	Neural convolutional network	MSSI, RMSE, others
	[87]	2020	MRI	Median filter, deep neural network	Matrix of confusion, others
	[88]	2021	PET	Linear statistical model	Mean, maximum, others
	[89]	2020	CT, MRI	Gaussian filter and histogram equalization	MSE, PSNR and SSIM
	[90]	2020	CT	Deep learning algorithm	ROC curve, sensitivity, and specificity
	[91]	2020	CT	Deep learning software	Sensitivity, specificity, predictive value
	[92]	2020	MRI, X-rays	Statistical methods	CLAHE, SSR, Fuzzy-II, DOTHE and BRISQUE
	[93]	2020	CT	Neural convolutional network	Precision, sensitivity, specificity, and ROC
	[94]	2019	MRI	Neural network	PSNR, SSIM and NMI
Colon	[95]	2019	CT, MSCT	Adaptive statistical iterative reconstruction	First- and second-order statistics
Heart	[96]	2022	PET, CT	Machine learning and Deep learning	Specificity and sensitivity
	[97]	2022	CT	The function of similarity	PSNR, entropy, MAE, MSE and others
	[98]	2021	CT	Adaptive filter	SNR, CNR, Anova
	[99]	2021	MRI	Selective binary set of levels	DC, RMSE, MHD
	[100]	2019	CT	Automated software system	Jaccard index, Dice coefficient
Kidney	[101]	2022	CT	Transference learning	Precision, sensitivity and specificity
	[102]	2021	US	Technique for characteristics extraction	PSNR, MSE
	[103]	2021	CT	Quantitative texture analysis	Precision, specificity, others
	[104]	2020	CT	Texture analysis, deep learning	Average, kurtosis, entropy, others
Rectum	[105]	2019	MRI	Smoothing, Laplacian and Gaussian filters	Concordance correlation coefficient
Pelvis	[106]	2021	CT, MRI	Deep learning architectures	MAE, ME, SSIM, PSNR
	[107]	2020	CT	Selective, adaptive and bilateral mean filter	Transfer function modulation
	[108]	2019	MRI	Mean, median, Wiener, and adaptive filters	PSNR and RMSE
	[109]	2019	CT	Thresholding, median, and gradient magnitude	Precision
Liver	[110]	2019	MSCT	Median filter, saturation, gradient magnitude	Dice coefficient
Lung	[111]	2021	CT, X-rays	Hybrid strategy based on a CNN and the AdaBoost	Precision
	[112]	2021	CT	Wavelet function	PSNR
	[113]	2021	CT	Neural network	Sensitivity
	[114]	2021	CT	Neural convolutional network	Precision, Dice Coefficient, Sensitivity
	[115]	2021	CT	Adaptative deep network and Wasserstein network	PSNR, SSIM
	[116]	2020	CT	Adaptative Wiener filter	Jaccard index and others
	[117]	2020	CT	DenseNet deep learning	Area under the curve
	[118]	2018	MRI	Wiener, median, Gaussian filter	Signal/noise ratio, others
Eyes	[119]	2021	DRIVE, STARE	Homomorphic and top-hat filters	Specificity, sensitivity, and precision
Teeth	[120]	2020	US	Median and Gaussian filter	PSNR
Multiple organs	[121]	2022	MRI, CT, PET, SPECT	Random walk guided filter and framelet domain	Spatial frequency, feature similarity, others
	[122]	2021	CT	Unsupervised network	Dice similarity coefficient, standard deviation
	[123]	2021	CT, MRI	Co-occurrence filter and local edges	Average, standard deviation, others
	[124]	2021	MRI	Genetic algorithm	PSNR, AMBE, SSIM, others
	[125]	2019	CT	3D region proposal network	Accuracy, overlapping ratio, others
Phantom	[126]	2020	CT, X-rays	Poisson's reconstruction method	RMSE, coefficient of variation
	[127]	2019	CT	Enhanced image reconstruction technique	PSNR,SSIM
	[128]	2019	X-rays	Mean, median, and Gaussian	Average, standard deviation

literature for MSCT image preprocessing and the evaluation metrics used [129].

Likewise, once the information in the specialized literature presented in this section has been reviewed and analyzed, a classification is made of the main preprocessing techniques based on statistical models either during the filtering stage or through the application of evaluation metrics and organized according to the organ of interest, as shown in Table 3.

In [73], the quality of abdomen and brain images was assessed using filtering techniques that included mean, Gaussian, median, and minimum filters. The techniques were evaluated based on the MSE and SSIM. The results demonstrated that the averaging filter performed better than others filters in terms of image quality enhancement.

Besides, [74] conducted a comparative study using eight filters – mean, median, Kuan, Lee, Frost, adaptive homomorphic, Wiener, and anisotropic diffusion – for the removal of speckle noise in medical images. A set of five quality metrics were used to assess the performance of the filters. Frost and adaptive homomorphic filters showed the best results.

Likewise, in [75], a forward projection technique was used to reduce streak artifacts caused by low photon counts in abdominal and thoracic images. The technique considers numerical projection, adaptive filtering, and reconstruction based on the processed sinogram

on synthetic images. The results were comparable to those of other iterative reconstruction techniques.

In [76], a set of filtering techniques were assessed based on their ability to reduce artifacts and Gaussian and speckle noise present in sinograms prior to the image reconstruction process. The set of filters included Gaussian, mean, Wiener, and bilateral filters. The latter exhibited the best performance in terms of the elimination of noise with respect to the reference image.

In [77], a bilateral, bidirectional, and 3D filtering technique was developed on low-dose images to compare edge-preserving noise reduction. The parameters were obtained empirically and exhibited noise reduction and better edge preservation.

Moreover, [78] presents an approach to predict the growth of abdominal aortic aneurysms using a longitudinal imaging dataset. The predictive ability of the method was assessed via principal component analysis.

In [79], a model was developed based on convolutional neural networks and recurrent networks for the detection of intracranial hemorrhage on noncontrast medical images. The precision, sensitivity, and specificity statistics of the model showed excellent diagnostic accuracy.

In [80], a filtering technique combining the edge-preserving median filter and a weighted scoring of the sparse nonlocal regularization algorithm were developed to remove impulsive and Gaussian noises in low-dose images. The experimental results showed that the proposed algorithm reduced mixed noise and preserved the information on the edges well.

Likewise, [81] presents the main applications of artificial intelligence, in particular, deep learning algorithms, and the fundamental architectures used in image pre-processing obtained through radioactive tracers.

In [82], a method involving the pre-processing, segmentation, and extraction of morphological characteristics of images was developed for the detection and classification of human brain tumors. High-pass and median filters were applied to reduce noise in the images, and WT and kernel support vector machine were applied to extract features from the images.

Similarly, [83] presents a technique based on a Gaussian filter and histogram equalization for noise elimination and contrast enhancement in images pertaining to different databases using MATLAB simulation. To assess the technique, a set of metrics including MSE, PSNR, similarity index, and quality index were applied, yielding favorable results.

A multimodal strategy for medical image fusion is presented in [84], which is based on the segment graph filter. In this strategy, the source images are decomposed into base and detail images. The base images are merged by applying a normalized Shannon entropy rule, whereas the detailed images are merged using a method based on sparse representation. Finally, the merged base and detailed images are combined. To assess the strategy, five metrics were applied, and the results were comparable to those of existing techniques.

On the other hand, [85] introduces an integrated web system, based on neural networks, for the pre-processing and automatic detection of brain hemorrhage and tissue classification in medical images. The entire database is stored on the main server and information pertaining to each patient is recorded on smart cards. The algorithm compares the full image on the myocardial perfusion map or the infarct detection and quantification results. This method can considerably facilitate specialists' workflow and prevent the redundancy of additional scan studies.

A multimodal medical image fusion system, based on multiscale decomposition with convolutional neural networks and sparse representation, is presented in [86]. This technique incorporates a smoothing filter for multimodal image decomposition and a set of statistical techniques during the fusion and reconstruction stages, achieving optimal performance in terms of visual consistency and quantitative analysis.

The hybrid technique developed in [87] considers statistical techniques, such as median filter, discrete wavelet transform, mean, standard deviation, asymmetry, and deep neural network, for the preprocessing, extraction, feature reduction, and classification of brain magnetic resonance images. The technique showed optimum performance compared with other image analysis techniques.

In [88], a generalized statistical linear model was developed for multiframe data bootstrapping in patients with brain and breast cancer. In this model, kinetic maps and uncertainties associated with data regarding fluorodeoxyglucose and fluorothymidine use were obtained using the bootstrapping technique. The performance of the model was consistent with that of theoretical statistical models.

A fusion approach was introduced in [89], which employs integrated anisotropic and nonlinear filtering with image statistics. This approach demonstrated better image quality compared with traditional image fusion algorithms.

In addition, [90] presents a study aimed at assessing the feasibility of a deep learning algorithm for artificial neural networks indicated for the detection of intracranial hemorrhage and the classification of its subtypes, without the need for a convolutional neural network. The performance of this approach was compared with that of a fully 3D deep learning approach, yielding a value of 0.859 on the ROC curve and a sensitivity and specificity of 78.0% and 80.0%, respectively.

In [91], a deep learning software was developed to detect acute intracranial hemorrhage in noncontrast images. The performance of the software was evaluated based on its sensitivity, specificity, PPV, negative predictive value, and precision statistical value. The software exhibited variability in terms of the location of the patient.

In [92], presents an algorithm that combines image processing concepts and statistical methods, aimed at enhancing contrast in medical imaging. The proposed algorithm showed good performance in image contrast enhancement compared with four other techniques.

Moreover, in [93], a learning system with deep neural network architecture was developed based on short-term memory and convolutional neural networks for the accurate and efficient detection of intracranial hemorrhages. The network was assessed by subjective comparison with the assessment made by the clinical specialist.

A comparative study in [94] evaluated four Rician denoising models and a wide range of noise levels using a neural network on a small image sample. The proposed denoising models outperformed existing techniques in terms of PSNR, structure similarity index metrics, and normalized mutual information.

In [95], a study was conducted to determine whether adaptive statistical iterative reconstruction affects the quantification of radiomic features in primary colorectal cancer in single-slice and multislice images in a cohort of 32 patients. Several measures including mean, standard deviation, skewness, kurtosis, energy, and entropy were calculated using multilevel linear regression. The results showed that radiomic analysis of CT images was affected by increased iterative reconstruction.

Likewise, [96] presents an artificial intelligence study based on artificial neural networks for the acquisition, reconstruction, and automatic segmentation of cardiac images. The study showed that a high degree of precision can be achieved in predicting cardiovascular events.

In [97], four variants of a filter based on a similarity criterion (complete, main, residual 1, and residual 2) were compared to enhance the information contained in cardiac images. The technique was compared using synthetic images and clinical cardiac imaging studies. Residual criterion 1 showed the best performance.

In [98], a model-based adaptive filter was suggested for the assessment of noise, sharpness, and quality of CT coronary angiography images using filtered back projection and adaptive statistical iterative reconstruction in the reconstruction of the coronary dataset. Compared with conventional techniques, noise reduction and image quality enhancement resulted in no changes in sharpness.

[99] presents a deformable geometric approach controlled by topological constraint, which uses a variant of the set of binary levels and selective Gaussian filtering for the segmentation of cardiac magnetic resonance images. Optimal global or local segmentations can be obtained using this approach.

Similarly, [100] developed an automated software for the segmentation of abdominal aortic aneurysms and the vascular system using an image dataset. The technique involves a pre-processing stage that includes Gaussian, median, and bilateral filters, among others, along with active contour methods for segmenting 2D and 3D regions. Segmentation results were evaluated using overlap-, volume-, and surface distance-based metrics. The median filter exhibited the best performance in terms of image quality enhancement and computational efficiency.

In [101], an automated image classification technique, which is based on transfer learning for kidney stone detection in medical imaging, was evaluated. For the extraction of features, iterative neighborhood component analysis and a cross-validation strategy were applied to assess the accuracy of the technique. The results showed > 99% accuracy.

In [102], presents a technique that utilizes high-pass filtering intended to estimate the level of speckle noise based on the extraction of characteristics of images contaminated with noise. The characteristics extracted are used to train the support vector regression model. The experimental results proved that the proposed technique exhibited better performance than existing techniques in terms of mean absolute deviation and execution time.

An automated technique is presented in [103], which considers a vector of characteristics for the quantitative analysis of the texture and classification of kidney lesions in medical imaging. The performance of the technique was calculated by metrics based on statistics of precision, specificity, sensitivity, and area under the curve of characteristics. The technique demonstrated good performance in terms of the classification of kidney lesions.

A quantitative study in [104] used texture analysis and deep learning techniques to predict the location of primary aldosteronism in noncontrast images. The study analyzed statistical filters such as a Laplacian or Gaussian filter with various spatial scale factors and logistic regression analysis. This analysis showed a favorable prediction capacity among some of the texture characteristics and the aldosterone production performance of the adrenal gland in patients with primary aldosteronism.

Similarly, [105] presents an exploratory study on images extracted from the diffusion coefficient maps of 56 patients with rectal cancer to extract reproducible delineation and texture characteristics in the previously filtered images. Rstudio and Python were used for statistical analysis using correlation coefficients, re-clustering, resampling, and smoothing using Laplacian and Gaussian pre-processing filters.

An atlas-based method was developed by [106] to compare different deep learning architectures (eCNN, U-Net, GAN, V-Net, and Res-Net) for the generation of synthetic CT images from magnetic resonance images. To measure the performance of each of the techniques, statistical metrics including mean error, MAE, Pearson correlation coefficient, SSIM, and PSNR were obtained, eCNN and ResNet showed the best performance.

In [107], a selective mean filter was evaluated in terms of its ability to reduce the noise present in synthetic images. During preprocessing, an adaptive mean filter and abilateral filter were applied. The results showed significant noise reduction and preservation of the spatial resolution of the image.

In [108], a set of digital filters that consider mean, median, Wiener, and adaptive filters were used to remove different levels of Gaussian noise, salt and pepper noise, and speckle noise. Some statistics such as the MSE were applied to compare the performance of the proposed filtering techniques.

Likewise,[109] developed a computational technique to characterize a pathological ovary in medical imaging. For pre-processing, preliminary thresholding and median and gradient magnitude filters were applied. Subsequently, the region-growing algorithm was applied to extract the 3D morphology of the pathological ovary. The implementation of the technique showed promising results.

Similarly, [110] presents an automated strategy that considers a pre-processing phase using a digital filter bank to reduce the effects of noise and artifacts. Later, in the second phase, an intelligent operator was used for liver detection based on the least-squares support vector to generate both the liver morphology and volume. Compared with manual segmentation, the proposed strategy proved to be efficient, with a Dice coefficient of 0.92.

A hybrid strategy is presented in [111], based on a convolutional neural network and the AdaBoost classification algorithm for the identification of the SARS-CoV-2 in lung images. The hybrid algorithm enhances the precision and ability to classify and predict the virus.

In [112], a comparative study of the performance of different wavelet functions was conducted for the removal of noise in images, aiming to detect coronavirus pneumonia in patients with COVID-19. The results indicated that the wavelet functions exhibited good performance in terms of noise removal.

In [113], an automatic detection system for the classification and 3D reconstruction of pulmonary nodules in CT images was developed based on morphological characteristics for neural network training. To determine the volume of the nodule and perform 3D reconstruction, the marching cube algorithm and Riemann integral formula were used. The results showed that the technique was reliable for the classification, detection, and segmentation of pulmonary nodules.

In [114], presents a hybrid technique for lung segmentation in medical imaging that uses a convolutional neural network based on mask regions and processing techniques. This technique can produce lung segmentations with 99% accuracy in several lung image datasets.

In [115], an adaptive deep network was developed and trained by introducing anatomy object labels containing previous anatomical information from low-dose images and augmented Wasserstein network to preserve more structural details. This enabled the network to achieve better performance.

In [116], an automatic detection system for the classification and 3D reconstruction of pulmonary nodules in CT images was developed based on morphological characteristics for neural network training. To determine the volume of the nodule and perform 3D reconstruction, the marching cube algorithm and Riemann integral formula were used. The results showed that the technique was reliable for the classification, detection, and segmentation of pulmonary nodules.

In [117], an image pre-processing technique was developed based on deep learning with a sparse matrix profile for the detection of abnormalities in chest images in SARS-CoV-2 cases. SARS-CoV-2 and non- SARS-CoV-2 images were compared using statistical measures. The technique enabled the detection of abnormal pixels in chest images, thereby making it possible to distinguish patients with and without SARS-CoV-2.

Similarly, in [118], a pre-processing technique was developed for denoising and improving the contrast and quality of the information contained in lung images using a set of filtering techniques, such as Wiener, median, and Gaussian filters. The median filter exhibited the best performance and significantly enhanced the intensity of the pixels and the quality of the image.

A robust strategy was developed in [119], which involved the preprocessing and segmentation of thin and thick retinal blood vessels for the detection of eye diseases in fundus images corresponding to two databases: DRIVE and STARE. An optimized set of top-hat and homomorphic filters was implemented. The technique achieved good performance compared with other current techniques.

Further, in [120], a filtering technique combining the median filter and the Gaussian filter to remove speckle noise was developed.

The filters were assessed in terms of PSNR statistics, and the results demonstrated successful noise reduction in the images.

A multimodal medical image fusion technique was developed in [121] that used a gradient domain-guided filtering technique as well as side-window filtering in the frame transformation domain. This technique outperformed all existing techniques in terms of objective assessment results and visual performance.

Likewise, in [122], a method without manual annotations, based on an unsupervised network, was developed for medical imaging pre-processing. The method was trained with 1030 tomographies. Compared with other supervised networks, the score obtained using the proposed method was significantly higher.

On the other hand, in [123], a multimodal medical image fusion method was developed for high and low-frequency components in the shearlet domain. At high frequencies, the technique combines base layers and detail layers using the local edge approach and this technique is merged with a co-occurrence filter, whereas at low frequencies, a technique based on a modified Laplacian filter, which preserves edges, is used. The results showed that edges, textures, and contrast were well maintained and preserved.

In [124], an adaptive histogram equalization technique was developed based on a genetic algorithm, histogram, and modified probability density function, wherein the exposure threshold and optimal threshold to preserve brightness and reduce information loss in images were used. The experimental results were promising compared with those of other existing techniques.

In [125], a method for localizing multiple organs on images was developed, wherein an efficient 3D region proposal network and a new backbone architecture were used, which generate high-resolution feature maps for small-organ localization. During processing, the method achieved a high accuracy of detection and localization of body organs and the head.

In addition, [126] presents a reconstruction technique based on Poisson statistics that explains the nonlinearities resulting from the hardening of the X-ray beam. The proposed technique does not require preliminary segmentation. The results demonstrated a decrease in beam hardening and dark bands.

Likewise, an enhanced image reconstruction technique was developed in [127] by incorporating a regularization term for bilateral edge preservation and a noise reduction method in the early construction phase. The proposed technique showed an improvement in the signal-to-noise ratio as it could control the noise in the initial stage.

In [128], a statistical assessment method was developed, along with a denoising technique for a sequence of images. Statistical parameters including mean, standard deviation, and signal-to-noise ratio were used to generate the noise profile in the phantoms. At a later stage, denoising in the image sequences was performed using spatial domain filters and mean, median, and Gaussian filters. The filters showed good performance in removing noise and enhancing image quality.

The Table 3, shows a description of the papers screened, reviewed, and classified according to imaging modality. The most used imaging modalities in pre-processing are presented: CT, MSCT, MRI, US, X-ray, PET, and SPECT. The statistical pre-processing techniques used in specialized literature are also presented. In addition, there is a section with the main metrics for the assessment of the quality of the information contained in the images that have been previously pre-processed, including PSNR, MSE, SSIM, root mean square error (RMSE), MAE, AMBE, Dice coefficient, JAC, confusion matrix, variance, maximum, mean, entropy, correlation, and others.

A total of 56 papers from the last 5 years (2018–2020) were screened, of which 50 were full-length articles and 6 were conference proceedings addressing the main statistical techniques applied to medical imaging, both in the pre-processing and segmentation stages. The papers were published in high-impact academic journals, as per the SCImago Journal Rank classification. Of the papers selected, 24 were published in Q1 journals, 16 in Q2 journals, 4 in Q3 journals, and 6 in Q4 journals and 6 were conference proceedings.

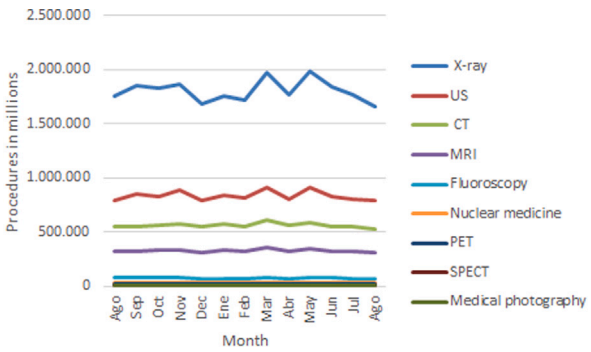

Fig. 7. Monthly distribution of NHS procedures by imaging modality from august 2021 to august 2022.

4. Discussion

The widespread adoption of advanced imaging modalities, particularly Multi-slice Computed Tomography (MSCT), is transforming clinical practice by providing enhanced diagnostic precision and supporting complex medical procedures. While X-ray imaging continues to be favored for its lower cost, there is an undeniable shift towards digital imaging modalities like CT scans, which offer superior detail and accuracy. This trend is clearly demonstrated in recent data from the English National Health Service (NHS) as shown in Fig. 7, which reported 43.9 million diagnostic imaging tests in a single year. Among these, X-rays were the most frequently performed, followed by ultrasound (US), computed tomography (CT), and magnetic resonance imaging (MRI). The increase in the use of these modalities, particularly CT, reflects the growing demand for high-quality medical images as healthcare services return to normalcy post-pandemic [130].

In the studies reviewed, statistical pre-processing techniques such as median filters, neural networks, and Gaussian filters, often based on deep learning, have been shown to significantly improve the quality of CT images by reducing noise and correcting artifacts.

As detailed in the Table 3, these techniques have been widely used across various imaging modalities, but CT images, in particular, have been the focus of 53% of the studies, as illustrated in Table 5 and Fig. 8. This heavy emphasis on CT images highlights the critical role that this modality plays in medical imaging, especially for complex diagnostic and surgical procedures involving the brain, lungs, and abdomen. However, while these techniques are effective, their robustness can vary depending on the dataset and the specific image artifacts encountered.

The methodological rigor in the application of these pre-processing techniques is noteworthy. Studies have consistently employed a range of statistical methods tailored to the specific challenges presented by different imaging modalities. The comparative analysis of techniques, as depicted in the Table 7 and Fig. 10, reveals that median-based filters are among the most frequently employed due to their simplicity and effectiveness in reducing noise. However, the rise of neural networks and deep learning-based approaches marks a significant evolution in the field, offering more sophisticated solutions that can adapt to complex patterns in medical images. These advancements underscore the ongoing innovation in the field, as researchers continue to push the boundaries of what is possible in medical image pre-processing.

A crucial factor influencing the choice of imaging modality is the type of disease or condition being diagnosed, as evidenced by the data in the Table 4, which details the diagnostic imaging activity for NHS patients. For instance, imaging modalities like CT and MRI are often preferred for diagnosing conditions such as brain, lung, and abdominal cancers due to their superior resolution and ability to capture detailed images of soft tissues. The increased reliance on these modalities for serious health conditions highlights the critical role that high-quality

Table 4
Diagnostic imaging activity in England for NHS patients from august 2021 to august 2022.

Month	X-ray	US	CT	MRI	Fluoroscopy	Nuclear Medicine	PET	SPECT	Medical Photography	Total
Aug	1.754.390	790.235	548.325	313.800	72.690	26.485	18.455	3.705	4.270	3.532.360
Sep	1.847.755	850.880	551.855	318.405	78.055	28.255	20.465	3.890	4.695	3.704.255
Oct	1.828.325	831.030	562.055	330.650	74.755	27.380	21.155	4.005	4.760	3.684.110
Nov	1.862.405	887.170	569.925	329.490	79.800	29.520	20.495	4.175	4.770	3.787.745
Dec	1.681.300	794.485	550.685	303.555	70.550	25.400	18.440	3.815	4.805	3.453.030
Jan	1.752.515	832.365	572.515	327.790	71.480	26.740	20.435	3.885	4.750	3.612.475
Feb	1.713.435	809.785	547.830	315.755	72.360	25.715	20.205	3.675	4.655	3.513.405
Mar	1.970.995	913.005	608.115	350.970	81.980	30.405	21.905	4.485	4.900	3.986.765
Apr	1.765.845	799.965	560.880	323.780	69.895	25.660	19.455	3.140	4.435	3.573.060
May	1.977.975	905.150	586.075	347.900	79.765	29.470	21.775	3.405	5.110	3.956.630
Jun	1.837.080	828.805	552.860	325.180	73.280	26.820	20.475	3.370	4.765	3.672.635
Jul	1.768.850	800.900	550.615	325.130	70.815	26.170	20.695	3.230	3.840	3.570.240
Aug	1.652.375	784.585	522.105	307.195	68.415	25.285	19.570	3.030	4.120	3.386.685
Total	21.658.855	10.038.130	6.735.510	3.905.805	891.145	326.825	245.065	44.100	55.605	43.901.035

Table 5
Imaging modalities most frequently reported in preprocessing literature.

Modality	Number of reports
CT	30
CT and others	5
X-ray	4
MRI	9
PET	2
SPECT	2
US	3
Others	1

Table 6
Anatomical targets of image preprocessing studies: a focused review.

Organ	Number of reports
Abdomen	6
Brain	16
Heart	5
Kidney	4
Colon	1
Rectum	1
Pelvis	4
Liver	1
Lungs	8
Eyes	1
Teeth	1
Multiple Organs	5
Phantom	3

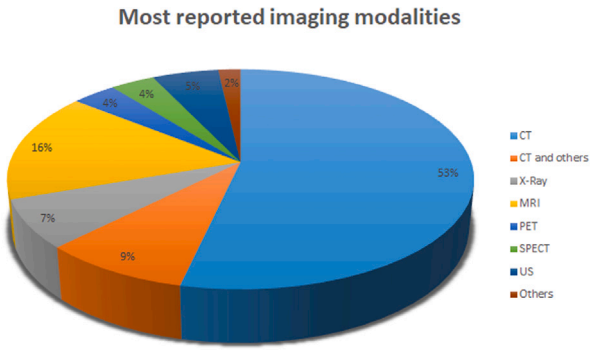

Fig. 8. Prevalence of imaging modalities in preprocessing studies: a summary chart.

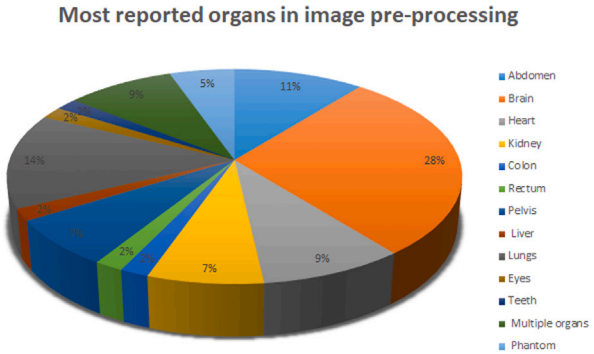

Fig. 9. Organ systems most frequently targeted in image preprocessing research.

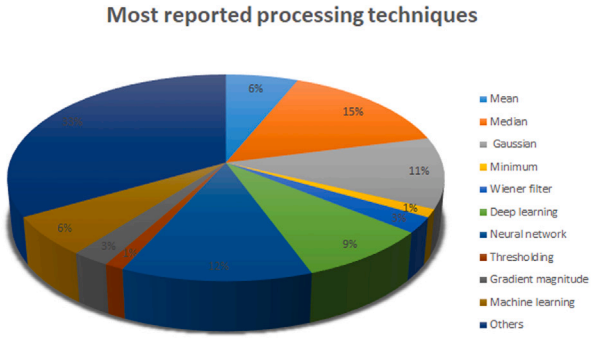

Fig. 10. Preprocessing techniques most reported in the literature: a statistical breakdown.

medical imaging plays in clinical decision-making. This is particularly important in complex cases where the precision of the imaging technique can directly impact the accuracy of the diagnosis.

Another critical aspect highlighted in the literature is the importance of evaluation metrics in validating the effectiveness of pre-processing techniques. As shown in Table 8 and Fig. 11, metrics such as PSNR, SSIM, and MSE are essential for assessing improvements in image quality. However, the selection of appropriate metrics is not straightforward, as different metrics may respond differently to various types of image degradation. For instance, while PSNR is widely used, it may not fully capture perceptual differences that are critical in clinical contexts. Therefore, a combination of metrics is often necessary to gain a comprehensive understanding of how pre-processing affects image quality. This layered approach to evaluation ensures that the techniques not only perform well in theory but also translate into meaningful improvements in clinical practice.

Despite these advancements, significant challenges remain, particularly regarding the generalizability of these techniques across different imaging modalities. One key limitation is the reliance on synthetic or idealized data in many studies, which may not fully capture the complexities of real-world medical images. Additionally, as highlighted in Table 9 and Fig. 12, biases can arise from the over-representation of CT images in the literature, which could skew perceptions of the

Table 7
Preprocessing techniques most reported in the literature: a detailed categorization.

Ref.	F1	F2	F3	F4	F5	F6	F7	F8	F9	F10	F11
[73]	x	x	x	x	–	–	–	–	–	–	–
[74]	x	x	–	–	–	–	–	–	–	–	x
[75]	–	–	–	–	–	–	–	–	–	–	x
[76]	–	x	x	–	–	–	–	–	–	–	x
[77]	–	–	–	–	–	–	–	–	–	–	x
[78]	–	–	x	–	–	–	–	–	–	–	–
[79]	–	–	–	–	–	–	x	–	–	–	–
[80]	–	x	–	–	–	–	–	–	–	–	–
[81]	–	–	–	–	–	x	–	–	–	–	–
[82]	–	x	–	–	–	–	–	–	–	–	x
[83]	–	–	x	–	–	–	–	–	–	–	x
[84]	–	–	–	–	–	–	–	–	–	–	x
[85]	–	–	–	–	–	–	–	–	–	x	–
[86]	–	–	–	–	–	–	x	–	–	–	–
[87]	–	x	–	–	–	–	x	–	–	–	–
[88]	–	–	–	–	–	–	–	–	–	–	x
[89]	–	–	x	–	–	–	–	–	–	–	–
[90]	–	–	–	–	–	x	–	–	–	–	–
[91]	–	–	–	–	–	x	–	–	–	–	–
[92]	–	–	–	–	–	–	–	–	–	–	x
[93]	–	–	–	–	–	–	x	–	–	–	–
[94]	–	–	–	–	–	–	x	–	–	–	–
[95]	–	–	–	–	–	–	–	–	–	–	x
[96]	–	–	–	–	–	–	–	–	–	x	–
[97]	–	–	–	–	–	–	–	–	–	–	x
[98]	–	–	–	–	–	–	–	–	–	–	x
[99]	–	–	–	–	–	–	–	–	–	–	x
[100]	–	–	–	–	–	–	–	–	–	x	x
[101]	–	–	–	–	–	–	–	–	–	–	x
[102]	–	–	–	–	–	–	–	–	–	–	x
[103]	–	–	–	–	–	–	–	–	–	–	x
[104]	–	–	–	–	–	x	–	–	–	–	x
[105]	–	–	x	–	–	–	–	–	–	–	x
[106]	–	–	–	–	–	x	–	–	–	–	–
[107]	x	–	–	–	–	–	–	–	–	–	x
[108]	x	x	–	–	x	–	–	–	–	x	–
[109]	–	x	–	–	–	–	–	x	x	–	x
[110]	–	x	–	–	–	–	–	–	x	x	–
[111]	–	–	–	–	–	–	x	–	–	–	x
[112]	–	–	–	–	–	–	–	–	–	–	x
[113]	–	–	–	–	–	–	x	–	–	–	–
[114]	–	–	–	–	–	–	x	–	–	–	–
[115]	–	–	–	–	–	–	x	–	–	–	x
[116]	–	–	–	–	–	x	–	–	–	–	–
[117]	–	–	–	–	–	x	–	–	–	–	–
[118]	–	x	x	–	x	–	–	–	–	–	–
[119]	–	–	–	–	–	–	–	–	–	–	x
[120]	–	x	x	–	–	–	–	–	–	–	x
[121]	–	–	–	–	–	–	–	–	–	–	x
[122]	–	–	–	–	–	–	x	–	–	–	–
[123]	–	–	–	–	–	–	–	–	–	–	x
[124]	–	–	–	–	–	–	–	–	–	–	x
[125]	–	–	–	–	–	–	–	–	–	–	x
[126]	–	–	–	–	–	–	–	–	–	–	x
[127]	–	–	–	–	–	–	–	–	–	–	x
[128]	x	x	x	–	–	–	–	–	–	–	–
Total	5	12	9	1	2	7	10	1	2	5	27

efficacy of these techniques when applied to other modalities like MRI, X-ray, and US. Overcoming these limitations will require the development of more robust algorithms that can handle a broader range of image imperfections and are applicable across diverse medical imaging contexts.

Moreover, the clinical relevance of these pre-processing techniques is profound, particularly in enhancing the quality of images used in critical procedures. As shown in Table 6 and Fig. 9, high-quality imaging is essential for accurately diagnosing and treating conditions affecting vital organs such as the brain, lungs, and abdomen. The integration of advanced pre-processing techniques into clinical workflows not only improves diagnostic accuracy but also enhances the outcomes of surgical procedures, where precision is crucial. However, these advancements come with technological implications, as the increased computational demands of sophisticated algorithms may require upgrades to existing medical imaging infrastructure. Healthcare providers must be prepared to invest in the necessary hardware and software to fully leverage these advancements.

Furthermore, the technological implications of these advancements should not be underestimated. The pre-processing techniques discussed require varying levels of computational power, and as more sophisticated methods like deep learning-based filters become prevalent, the demand for specialized hardware and software will increase. This shift necessitates a reevaluation of current medical imaging infrastructure to ensure compatibility with the latest pre-processing techniques. Healthcare facilities may need to invest in more powerful computing systems or cloud-based solutions to manage the increased data processing requirements effectively. This aspect is particularly crucial for ensuring

Table 8
Quality assessment metrics for medical images: a guide to the most reported evaluations.

Ref.	M1	M2	M3	M4	M5	M6	M7	M8	M9	M10	M11	M12	M13	M14	M15
[73]	x	x	x	–	–	–	–	–	–	–	–	–	–	–	–
[74]	x		x	x	–	–	–	–	–	–	–	–	–	–	x
[75]	–	–	–	–	–	–	–	–	–	–	–	–	–	–	x
[76]	x	–	x	–	–	–	–	–	–	–	–	–	–	–	–
[77]	–	–	–	–	–	–	–	–	–	–	–	–	–	–	x
[78]	–	–	–	–	–	–	–	–	–	–	–	–	–	–	x
[79]	–	–	–	–	–	–	–	–	x	–	–	–	–	–	–
[80]	x	–	x	–	–	–	–	–	–	–	–	–	–	–	–
[81]	–	–	–	–	–	–	–	–	x	–	–	–	–	–	–
[82]	–	–	–	–	–	–	–	–	–	–	–	x	x	x	–
[83]	x	x	x	–	–	–	–	–	–	–	–	–	–	–	–
[84]	–	–	–	–	–	–	–	–	–	–	–	–	x	–	x
[85]	–	–	–	–	–	–	–	–	x	–	–	–	–	–	x
[86]	–	–	–	x	–	–	–	–	–	–	–	–	–	–	x
[87]	–	–	–	–	–	–	–	–	x	–	–	–	–	–	x
[88]	–	–	–	–	–	–	–	–	–	–	x	x	–	–	x
[89]	x	x	x	–	–	–	–	–	–	–	–	–	–	–	–
[90]	–	–	–	–	–	–	–	–	x	–	–	–	–	–	x
[91]	–	–	–	–	–	–	–	–	x	–	–	–	–	–	x
[92]	–	–	–	–	–	–	–	–	–	–	–	–	–	–	x
[93]	–	–	–	–	–	–	–	–	x	–	–	–	–	–	x
[94]	x	–	x	–	–	–	–	–	–	–	–	–	–	–	x
[95]	–	–	–	–	–	–	–	–	–	–	–	x	–	–	–
[96]	–	–	–	–	–	–	–	–	x	–	–	–	–	–	–
[97]	x	x	–	–	x	–	–	–	–	–	–	–	x	–	x
[98]	x	–	–	–	–	–	–	–	–	–	–	–	–	–	x
[99]	–	–	–	x	–	–	–	–	–	–	–	–	–	–	x
[100]	–	–	–	–	–	–	x	x	–	–	–	–	–	–	–
[101]	–	–	–	–	–	–	–	–	x	–	–	–	–	–	–
[102]	x	x	–	–	–	–	–	–	–	–	–	–	–	–	–
[103]	–	–	–	–	–	–	–	–	x	–	–	–	–	–	x
[104]	–	–	–	–	–	–	–	–	x	–	–	–	–	–	x
[105]	–	–	–	–	–	–	–	–	–	–	–	–	–	x	–
[106]	x	–	x	–	x	–	–	–	–	–	–	–	–	–	–
[107]	–	–	–	–	–	–	–	–	–	–	–	–	–	–	x
[108]	x	–	–	x	–	–	–	–	–	–	–	–	–	–	–
[109]	–	–	–	–	–	–	–	–	x	–	–	–	–	–	–
[110]	–	–	–	–	–	–	x	–	–	–	–	–	–	–	–
[111]	–	–	–	–	–	–	–	–	x	–	–	–	–	–	–
[112]	x	–	–	–	–	–	–	–	–	–	–	–	–	–	–
[113]	–	–	–	–	–	–	–	–	x	–	–	–	–	–	–
[114]	–	–	–	–	–	–	x	–	x	–	–	–	–	–	–
[115]	x	–	x	–	–	–	–	–	–	–	–	–	–	–	–
[116]	–	–	–	–	–	–	–	x	–	–	–	–	–	–	x
[117]	–	–	–	–	–	–	–	–	–	–	–	–	–	–	x
[118]	x	–	–	–	–	–	–	–	–	–	–	–	–	–	x
[119]	–	–	–	–	–	–	–	–	x	–	–	–	–	–	–
[120]	x	–	–	–	–	–	–	–	–	–	–	–	–	–	–
[121]	–	–	x	–	–	–	–	–	–	–	–	–	–	–	–
[122]	–	–	–	–	–	–	x	–	–	–	–	–	–	–	x
[123]	–	–	–	–	–	–	–	–	–	–	–	–	–	–	x
[124]	x	–	x	–	–	x	–	–	–	–	–	–	–	–	x
[125]	–	–	–	–	–	–	–	–	x	–	–	–	–	–	x
[126]	–	–	–	x	–	–	–	–	–	–	–	–	–	–	x
[127]	x	–	x	–	–	–	–	–	–	–	–	–	–	–	–
[128]	x	–	–	–	–	–	–	–	–	–	–	–	–	–	x
Total	19	5	12	5	2	1	4	2	17	0	1	3	3	2	17

that the benefits of these advanced techniques are fully realized in clinical settings.

Finally, the future of medical image pre-processing lies in the continued exploration of innovative approaches and the standardization of techniques and metrics. As indicated in the literature, there is a pressing need for the development of standardized protocols that can be universally applied across different imaging modalities. This standardization will not only improve the reproducibility of results but also facilitate the integration of these techniques into clinical practice on a broader scale. Future research should focus on addressing these gaps, particularly in refining algorithms to handle the unique challenges presented by different types of medical images and in establishing universally accepted evaluation metrics that can reliably measure improvements in image quality.

In brief, the reviewed studies provide compelling evidence of the progress being made in medical image pre-processing. The comprehensive analysis presented in Tables 3, 4, 5 - 9 and Figs. 8–12, underscores both the advancements and the challenges that lie ahead. As the field continues to evolve, the focus must remain on developing robust, standardized techniques that can be seamlessly integrated into clinical practice, ensuring that medical imaging continues to be a cornerstone of modern medicine, delivering the precision and reliability necessary for improving patient care and outcomes.

5. Conclusions

Statistical pre-processing techniques are diverse and varied, as are their uses for digital image processing based on the image acquisition

Table 9
Review criteria for evaluating preprocessing techniques in medical imaging literature.

Ref.	C1	C2	C3	C4	C5	C6	C7	C8	C9	C10	C11	C12	C13	C14
[73]	x	x	x	x	–	–	x	x	–	–	–	x	–	–
[74]	x	x	x	x	x	–	–	x	–	–	x	–	x	–
[75]	x	x	–	x	–	–	x	–	–	x	–	x	–	–
[76]	x	–	x	x	–	–	x	–	–	x	x	x	–	–
[77]	x	–	–	x	–	x	x	–	–	x	–	x	–	–
[78]	x	x	–	x	–	x	–	x	–	–	–	x	–	x
[79]	x	–	–	–	–	x	–	x	–	–	–	x	–	–
[80]	x	x	–	x	x	–	–	–	–	x	x	x	–	–
[81]	x	–	–	x	–	x	x	–	–	x	–	–	x	x
[82]	–	–	x	x	–	x	–	x	–	–	–	–	x	–
[83]	x	x	x	x	x	–	–	x	–	–	–	–	x	–
[84]	x	x	x	–	–	–	x	x	–	–	–	x	x	–
[85]	x	x	–	x	–	x	–	x	–	–	–	x	–	–
[86]	x	x	–	x	–	–	x	x	–	–	–	x	x	–
[87]	x	x	x	x	–	x	–	x	–	–	x	–	x	x
[88]	x	x	–	–	–	–	x	x	–	–	–	–	x	–
[89]	x	x	x	x	x	–	–	x	–	–	x	x	x	x
[90]	–	–	–	–	–	x	–	x	–	–	–	x	–	–
[91]	–	–	–	x	x	–	–	x	–	–	–	x	–	–
[92]	x	x	x	–	–	x	–	x	–	–	x	–	x	x
[93]	x	x	–	–	–	x	–	x	–	–	–	x	–	–
[94]	x	x	–	–	x	–	–	x	–	–	–	–	x	–
[95]	–	–	–	–	–	–	x	x	–	–	–	x	–	–
[96]	x	–	–	–	–	–	–	x	–	–	–	x	x	–
[97]	x	x	–	x	x	–	–	–	–	x	–	x	–	x
[98]	x	x	–	x	–	–	x	x	–	–	–	x	–	–
[99]	x	x	–	x	–	x	–	x	–	–	x	–	x	–
[100]	x	x	x	–	–	x	–	x	–	–	x	x	–	x
[101]	x	x	–	x	x	x	–	x	–	–	–	x	–	–
[102]	x	x	–	–	–	x	–	x	–	–	–	–	x	x
[103]	x	x	–	–	–	x	–	x	–	–	–	x	–	–
[104]	–	–	x	x	x	–	–	x	–	–	–	x	–	–
[105]	x	–	x	x	–	–	x	x	–	–	–	–	x	–
[106]	x	x	–	x	x	x	–	–	–	x	–	x	x	–
[107]	x	–	x	x	x	x	–	–	–	x	–	x	x	–
[108]	x	x	x	x	x	–	–	x	–	–	–	–	x	–
[109]	x	x	x	x	–	x	–	x	–	–	–	x	–	–
[110]	x	x	x	x	–	x	–	x	–	–	–	x	–	–
[111]	x	x	x	x	–	x	–	x	–	–	–	x	–	–
[112]	x	x	–	–	–	x	–	x	–	–	–	x	–	–
[113]	x	x	–	–	–	x	x	x	–	–	–	x	–	x
[114]	x	x	x	x	–	x	–	x	–	–	–	x	–	x
[115]	x	x	x	x	–	x	–	x	–	–	–	x	–	–
[116]	x	x	–	–	–	x	–	x	–	–	–	x	–	x
[117]	x	x	–	–	x	–	–	x	–	–	–	x	–	–
[118]	x	–	x	–	x	–	–	x	–	–	–	–	x	–
[119]	x	x	x	–	–	x	–	x	–	–	–	–	x	x
[120]	x	–	x	–	x	–	–	x	–	–	–	–	x	–
[121]	x	x	x	–	–	x	x	x	–	–	x	x	x	–
[122]	x	x	–	x	x	–	–	x	–	–	–	x	–	–
[123]	x	x	x	–	–	–	x	x	–	–	–	x	x	–
[124]	x	x	–	x	x	–	–	x	–	–	x	–	x	–
[125]	x	x	–	x	–	x	–	x	–	–	–	x	–	x
[126]	x	x	–	–	–	x	–	–	x	x	x	x	–	–
[127]	x	x	–	x	–	–	x	–	x	x	–	x	–	–
[128]	x	x	x	x	x	–	–	–	x	–	–	–	x	–
Total	51	42	25	34	18	29	15	45	3	10	11	39	25	13

modality and the imperfections inherent to each modality. In addition, metrics for evaluating the image quality are intended to provide a quantitative measure of the enhancement of the information contained in filtered images during the pre-processing or segmentation stage. Filtering techniques are assessed based on the enhancements they incorporate into the attributes and characteristics of the filtered image, such as sharpness, brightness, illumination, pixel intensity variation, background uniformity, texture, noise reduction, distortions, smoothing, and edge enhancement, among others. Techniques based on statistical foundations for the treatment and assessment of information quality enhancement in digital images are of particular importance.

Furthermore, based on the review of the 56 medical papers on image pre-processing listed in Table 3, the following conclusions can be drawn:

- CT, and in general, MSCT, are the most interesting imaging modalities in terms of the application of statistical techniques in medical image processing.
- Statistical filters based on median and neural networks; Gaussian filters; and filters based on deep learning, mean, and machine learning are among the most commonly used pre-processing statistical techniques for reducing imperfections in image information.

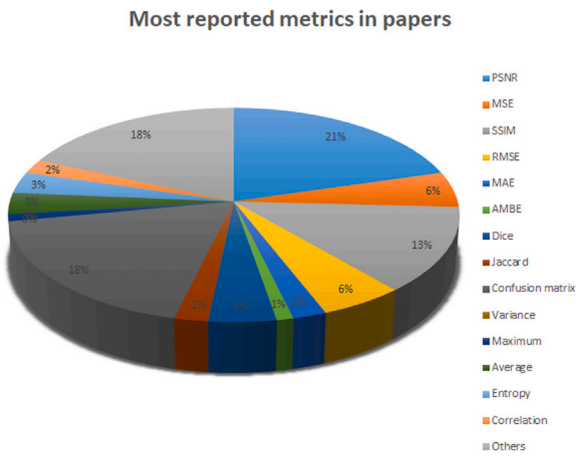

Fig. 11. Metrics most used to evaluate preprocessing techniques in medical imaging research.

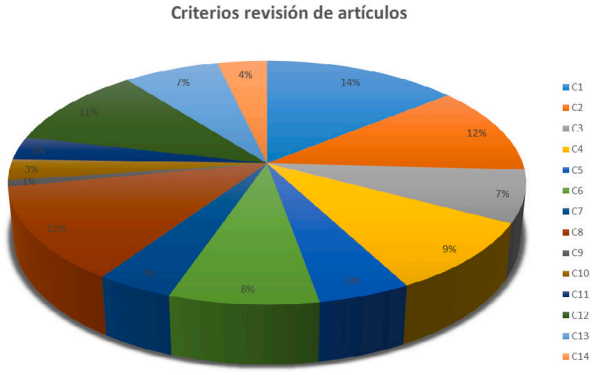

Fig. 12. Criteria applied in the review of techniques and metrics for medical image preprocessing.

- The metrics most widely used in studies consulted in this review that aimed to assess the quality of filters used for medical image pre-processing are as follows: PSNR, confusion matrix, SSIM, MSE, RMSE, MAE, JAC, correlation, AMBE, and maximum. It is important to note that most studies used more than one metric.
- In any pre-processing study, it is necessary to theoretically support, at least, the medical imaging modalities, pre-processing techniques, and metrics used for evaluation.

On the other hand, it can be stated that there is no uniform standard in terms of pre-processing techniques and metrics for the assessment of the quality of information contained in processed images. This study aims to provide a reference for consultation in terms of the most widely reported pre-processing techniques and metrics in specialized literature, so much so that the theoretical basis supporting a pool of techniques for both pre-processing and assessment metrics in medical imaging is presented.

Declaration of competing interest

The authors declare that they have no known competing financial interests or personal relationships that could have appeared to influence the work reported in this paper.

Data availability

Data will be made available on request.

Acknowledgments

The authors thank Crimson Interactive Pvt. Ltd. (Enago) – https://www.enago.com/es/ for their assistance in manuscript translation and editing.

References

[1] J. Stoitsis, I. Valavanis, S.G. Mougiakakou, S. Golemati, A. Nikita, K.S. Nikita, Computer aided diagnosis based on medical image processing and artificial intelligence methods, Nucl. Instrum. Methods Phys. Res. A 569 (2) (2006) 591–595.
[2] O. Valbuena, M. Vera, Y. Huérfano, E. Gelvez, J. Salazar, V. Molina, F. Sáenz, M.I. Vera, W. Salazar, Computational strategy for the segmentation of the aortic annulus in cardiac computed tomography images, J. Phys. Conf. Ser. 1160 (2019).
[3] R. Goldberg, R. Smith, J. Mottley, W. Ferrara, Ultrasound, in: J. Bronzino (Ed.), The Biomedical Engineering Handbook: Second Edition, Vol. 1, CRC Press LLC, Boca Raton, 2000, pp. 1247–1289.
[4] R. Reba, Nuclear medicine, vol. 270, no. 2, 1993, pp. 230–233.
[5] E. Garcia, T. Faber, J. Galt, C. Cooke, R. Folks, Advances in nuclear emission PET and SPECT imaging, IEEE Eng. Med. Biol. Mag. 19 (5) (2000) 21–33.
[6] A. Macovski, J. Pauly, J. Schenck, K. Kwong, D. Chesler, X. Hu, W. Chen, M. Patel, K. Ugurbil, S. Olly, Magnetic resonance imaging, in: J.D. Bronzino (Ed.), The Biomedical Engineering Handbook: Second Edition, Vol. 1, CRC Press LLC, Boca Raton, 2000, pp. 1174–1215.
[7] N. Dey, A. Ashour, A. Ashour, A. Singh, Digital analysis of microscopic images in medicine, J. Adv. Microsc. Res. 10 (2015) 1–13.
[8] J. East, L. Vleugels, P. Roelandt, P. Bhandari, G. Horgan, R. Kiesslich, G. Longcroft, A. Wilson, M. Dumonceau, Dvanced endoscopic imaging: European society of gastrointestinal endoscopy (ESGE) technology review, Endoscopy 48 (11) (2016) 1029–1045.
[9] D. Baim, Grossman's Cardiac Catheterization, Angiography and Intervention, Lippincott Williams and Wilkins, USA, 2006.
[10] A. Cournand, Cardiac catheterization. Development of the technique, its contributions to experimental medicine, and its initial application in man, Scand. Suppl. Med. Rec. 32 (1) (1975) 579–592.
[11] R. Gordon, R. Bender, G. Herman, Algebraic reconstruction techniques (ART) for three–dimensional electron microscopy and X–ray photography, J. Theoret. Biol. 29 (9) (1970) 471–482.
[12] W.A. Kalender, Computed Tomography: Fundamentals, System Technology, Image Quality, Applications, Publicis MCD Verlag, Munich, Germany, 2000.
[13] G. Wang, C. Crawford, Guest editorial: Multirow detector and cone–beam spiral/helical CT, IEEE Trans. Med. Imaging 19 (9) (2000) 817–820.
[14] G. Hounsfield, Computarized transverse axial scanning tomography: Part I, Br. J. Radiol. 1 (1973) 1016–1022.
[15] B. Ohnesorge, T. Flohr, C. Becker, A. Kopp, U. Schoepf, U. Baum, A. Knez, K. Klingenbeck, M. Reiser, Cardiac imaging by means of electrocardiographically gated multisection spiral CT: Initial experience, vol. 217, no. 2, 2000, pp. 564–671.
[16] T. Fuchs, M. Kachelriess, W. Kalender, Systems performance multislice spiral computed tomography, IEEE Eng. Med. Biol. 19 (5) (2000) 63–70.
[17] R. Kruger, X–ray Digital Cineangiocardiography, en Cardiac Imaging and Image Processing, MacGraw–Hill, USA, 1986.
[18] L. Kroft, A. De Roos, J. Geleijns, Artifacts in ECG–synchronized MDCT coronary angiography, vol. 189, no. 3, 2007, pp. 581–591.
[19] A. Maiera, L. Wigstrm, H. Hofmann, J. Hornegger, L. Zhu, N. Strobel, R. Fahrig, Three-dimensional anisotropic adaptive filtering of projection data for noise reduction in cone beam CT, Med. Phys. 38 (11) (2011) 5896–5909.
[20] A. Fakhre, R. Sami, Challenges and solutions in multimodal medical image subregion detection and registration, J. Med. Imaging Radiat. Sci. 50 (2019) 24–30.
[21] R. Zanella, P. Boccacci, L. Zanni, M. Bertero, Efficient gradient projection methods for edge-preserving removal of Poisson noise, Inverse Problems 25 (4) (2009) 1–24.
[22] R. Chan, K. Chen, Multilevel algorithm for a Poisson noise removal model with total–Variation regularization, Int. J. Comput. Math. (5) (2007) 1–18.
[23] M. Vera, A. Bravo, R. Medina, Description and use of three-dimensional numerical phantoms of cardiac computed tomography images, Data 7 (2022) 115.
[24] J. Hsieh, Image artifacts: Appearances, causes, and corrections, in: SPIE Press Computed Tomography: Principles, Design, Artifacts, and Recent Advances, Bellingham, WA, USA, 2003, pp. 167–240.
[25] J. Barrett, N. Keat, Artifacts in CT: Recognition and avoidance, Radiographics 24 (6) (2004) 1679–1691.
[26] G. Rubin, D. Paik, P. Johnston, S. Napel, Measurement of the aorta and its branches with helical CT, Radiology (206) (1998) 823–829.
[27] W. Pratt, Digital Image Processing, John Wiley & Sons Inc, USA, 2007.
[28] R. González, R. Woods, Digital Image Processing, Prentice Hall, USA, 2001.

[29] G. Arce, A general weighted median filter structure admitting negative weights, IEEE Trans. Signal Process. 46 (12) (1998) 3195–3205.
[30] M. Fischer, J. Paredes, G. Arce, Image sharpening for the world wide web, IEEE Trans. Image Process. 11 (3) (2002) 717–727.
[31] M. Fischer, J. Paredes, G. Arce, Image sharpeners using permutation weighted median filters, in: EUROSIP, Tampere, Finland, 2010, pp. 299–303.
[32] A. Buades, B. Coll, J. Morel, A review of image denoising algorithms with a new one, Multiscale Model. Simul. 4 (2) (2005) 490–530.
[33] P. Coupé, P. Yger, S. Prima, P. Hellier, C. Kervrann, C. Barillot, An optimized blockwise nonlocal means denoising filter for 3-D magnetic resonance images, vol. 27, no. 4, 2008, pp. 425–441.
[34] A. Bravo, J. Clemente, M. Vera, J. Avila, R. Medina, A hybrid boundary–region left ventricle segmentation in computed tomography, in: 5^{Th} VISAPP, Angers, France, 2010, pp. 107–114.
[35] M. Vera, A. Bravo, M. Garreau, R. Medina, Similarity enhancement for automatic segmentation of cardiac structures in computed tomography volumes, in: Engineering in Medicine and Biology Society,EMBC, 2011 Annual International Conference of the IEEE, Boston, USA, 2011, pp. 8094–8097.
[36] A. Bravo, M. Vera, Y. Huerfano Maldonado, Y. Hidalgo, A comprehensive study of a similarity criterion in cardiac computerized tomography images enhancement, Revista Facultad de Ingeniería Universidad de Antioquia (2020).
[37] G. Passarielo, F. Mora, Imágenes Médicas, Adquisición, Análisis, Procesamiento e Interpretación, Equinoccio Universidad Simón Bolivar, Venezuela, 1995.
[38] J. Rivest, P. Soille, S. Beucher, Morphological gradients, Electron. Imaging 2 (4) (1993) 326–336.
[39] Z. Yu, G. Wei, C. Zhen, T. Jing, L. Ling, Medical images edge detection based on mathematical morphology, in: Proceedings of the IEEE Eng. Med. Biol. 27th Annual Conference, Shanghai–China, 2005, pp. 6492–6495.
[40] R. Haralick, L. Shapiro, Computer and Robot Vision, vol. I, Addison–Wesley, USA, 1992.
[41] S. Mukhopadhyay, B. Chanda, A multiscale morphological approach to local contrast enhancement, Signal Process. 80 (4) (2000) 685–696.
[42] E. Pauwels, G. Frederix, Finding Salient Regions in images: Non–parametric clustering for image segmentation and grouping, vol. 18, no. 1–2, 1999, pp. 73–85, Special issue.
[43] H. Meijering, Image Enhancement in Digital X–Ray Angiography (Ph.D. thesis), Utrecht University, Netherlands, 2000.
[44] A. Fabijańska, Variance filter for edge detection and edge-based image segmentation, in: 2011 Proceedings of 7th International Conference on Perspective Technologies and Methods in MEMS Design, MEMSTECH 2011, 2011.
[45] T. Chen, Q. Wu, R. Rahmani, J. Hughes, A pseudo top-hat mathematical morphological approach to edge detection in dark regions, vol. 35, no. 1, 2002, pp. 199–210.
[46] G. Pajares, J. Cruz., Visión Por Computador. Imágenes Digitales Y Aplicaciones, RaMa, Madrid, España, 2001.
[47] J. Canny, Finding Edges and Lines in Images, Report 720 Massachusetts, MIT: Massachusetts Institute of Technology, 1983.
[48] J. Canny, A Computational Approach to Edge Detection, vol. PAMI–8, 1986, pp. 679–698.
[49] L. Jaya, R. Gopikakumari, IEM: A new image enhancement metric for contrast and sharpness measurements, Int. J. Comput. Appl. 79 (9) (2013) 1–9.
[50] C.E. Shannon, A mathematical theory of communication, Bell Syst. Tech. J. 27 (3) (1948) 379–423.
[51] B. Girod, What's wrong with mean-squared error, in: Digital Images and Human Vision, MIT Press, Cambridge, MA, USA, 1993, pp. 207–220.
[52] S. Gupta, R. Porwal, Appropriate contrast enhancement measures for brain and breast cancer images, Int. J. Biomed. Imaging 2016 (2016) 1–8.
[53] K. Panetta, E. Wharton, S. Agaian, Human visual system-based image enhancement and logarithmic contrast measure, IEEE Trans. Syst. Man Cybern. 38 (1) (2008) 174–188.
[54] B. Ridha Ilyas, M. Beladgham, K. Merit, A. taleb ahmed, Improved facial expression recognition based on DWT feature for deep CNN, Electronics 8 (2019) 324.
[55] R. Cárdenes, R. de Luis-García, M. Bach-Cuadra, A multidimensional segmentation evaluation for medical image data, Comput. Methods Programs Biomed. 96 (2) (2009) 108–124.
[56] H.-H. Chang, A.H. Zhuang, D.J. Valentino, W.-C. Chu, Performance measure characterization for evaluating neuroimage segmentation algorithms, NeuroImage 47 (1) (2009) 122–135.
[57] D. Blair, Information retrieval, J. Am. Soc. Inf. Sci. 30 (6) (1979) 374–375.
[58] L. Dice, Measures of the amount of ecologic association between species, Ecology 26 (3) (1945) 297–302.
[59] D. Martin, C. Fowlkes, D. Tal, J. Malik, A database of human segmented natural images and its application to evaluating segmentation algorithms and measuring ecological statistics, in: Proc. 8th Int'L Conf. Computer Vision, 2001, pp. 416–423.
[60] A. Taha, A. Hanbury, Metrics for evaluating 3D medical image segmentation: Analysis, selection, and tool, BMC Med. Imaging 15 (29) (2015) 1–28.
[61] W. Rand, Objective criteria for the evaluation of clustering methods, J. Amer. Statist. Assoc. 66 (1971) 846–850.
[62] L. Hubert, P. Arabie, Comparing partitions, J. Classification 2 (1985) 193–218.
[63] P. Viola, W. Wells, Alignment by maximization of mutual information, in: Proceedings of IEEE International Conference on Computer Vision, 1995, pp. 16–23.
[64] M. Meilă, Comparing clusterings by the variation of information, in: B. Schölkopf, M.K. Warmuth (Eds.), Learning Theory and Kernel Machines, Springer Berlin Heidelberg, Berlin, Heidelberg, 2003, pp. 173–187.
[65] P. Shrout, J. Fleiss, Intraclass correlations: Uses in assessing rater reliability, Psychol. Bull. 86 (2) (1979) 420–428.
[66] G. Gerig, M. Jomier, M. Chakos, Valmet: A new validation tool for assessing and improving 3D object segmentation, in: Medical Image Computing and Computer-Assisted Intervention, MICCAI, Springer, Berlin, Heidelberg, 2001, pp. 516–523.
[67] A.P. Bradley, The use of the area under the ROC curve in the evaluation of machine learning algorithms, Pattern Recognit. 30 (7) (1997) 1145–1159.
[68] A. Taha, A. Hanbury, An efficient algorithm for calculating the exact hausdorff distance, IEEE Trans. Pattern Anal. Mach. Intell. 37 (11) (2015) 2153–2163.
[69] M. Shapiro, M. Blaschko, On Hausdorff Distance Measures, Technical Report, Department of Computer Science, University of Massachusetts Amherst, 2004.
[70] P. Mahalanobis, On the generalized distance in statistics, in: Proceedings of the National Institute of Sciences (Calcutta), vol. 2, 1936, pp. 49–55.
[71] G. Mclachlan, Mahalanobis distance, Resonance 4 (1999) 20–26.
[72] M. Polak, H. Zhang, M. Pi, An evaluation metric for image segmentation of multiple objects, Image Vis. Comput. 27 (8) (2009) 1223–1227.
[73] H. Omer, N. Tamam, S. Alameen, S. Algadi, D. Thanh Tai, A. Sulieman, Elimination of biological and physical artifacts in abdomen and brain computed tomography procedures using filtering techniques, Saudi J. Biol. Sci. 29 (4) (2022) 2180–2186.
[74] M.N. Khan, A. Altalbe, Experimental evaluation of filters used for removing speckle noise and enhancing ultrasound image quality, Biomed. Signal Process. Control 73 (2022) 103399.
[75] S. Niwa, K. Ichikawa, H. Kawashima, T. Takata, S. Minami, W. Mitsui, Reduction of streak artifacts caused by low photon counts utilizing an image-based forward projection in computed tomography, Comput. Biol. Med. 135 (2021) 104583.
[76] M. Chillarón, V. Vidal, G. Verdú, Evaluation of image filters for their integration with LSQR computerized tomography reconstruction method, PLoS ONE 15 (3) (2020) e0229113.
[77] K. Ichikawa, H. Kawashima, M. Shimada, T. Adachi, T. Takata, A three-dimensional cross-directional bilateral filter for edge-preserving noise reduction of low-dose computed tomography images, Comput. Biol. Med. 111 (2019) 103353.
[78] H.N. Do, A. Ijaz, H. Gharahi, B. Zambrano, J. Choi, W. Lee, S. Baek, Prediction of abdominal aortic aneurysm growth using dynamical Gaussian process implicit surface, IEEE Trans. Biomed. Eng. 66 (3) (2019) 609–622.
[79] D. Alis, C. Alis, M. Yergin, C. Topel, O. Asmakutlu, O. Bagcilar, Y.D. Senli, A. Ustundag, V. Salt, S.N. Dogan, M. Velioglu, H.H. Selcuk, B. Kara, C. Ozer, I. Oksuz, O. Kizilkilic, E. Karaarslan, A joint convolutional-recurrent neural network with an attention mechanism for detecting intracranial hemorrhage on noncontrast head CT, Sci. Rep. 12 (2084) (2022).
[80] Q. Yuan, Z. Peng, Z. Chen, Y. Guo, B. Yang, X. Zeng, Edge-preserving median filter and weighted coding with sparse nonlocal regularization for low-dose CT image denoising algorithm, J. Healthcare Eng. 2021 (2021) 1–7.
[81] H. Arabi, A. AkhavanAllaf, A. Sanaat, I. Shiri, H. Zaidi, The promise of artificial intelligence and deep learning in PET and SPECT imaging, Eur. J. Med. Phys. 83 (2021) 122–137.
[82] S. Gobhinath, S. Anandkumar, R. Dhayalan, P. Ezhilbharathi, R. Haridharan, Human brain tumor detection and classification by medical image processing, ICACCS, in: 2021 7th International Conference on Advanced Computing and Communication Systems, vol. 1, 2021, pp. 561–564.
[83] K. Srinivasa Reddy, T. Jaya, De-noising and enhancement of MRI medical images using Gaussian filter and histogram equalization, Mater. Today: Proc. (2021).
[84] Q. Li, W. Wang, G. Chen, D. Zhao, Medical image fusion using segment graph filter and sparse representation, Comput. Biol. Med. 131 (2021) 104239.
[85] Y. Jiang, J. Liu, H. Sheng, High resolution image processing and CT perfusion imaging detection in patients with cerebral hemorrhage based on embedded system, Microprocess. Microsyst. 81 (2021) 103700.
[86] D.S. Shibu, S.S. Priyadharsini, Multi scale decomposition based medical image fusion using convolutional neural network and sparse representation, Biomed. Signal Process. Control 69 (2021) 102789.
[87] Z. Ullah, M.U. Farooq, S.-H. Lee, D. An, A hybrid image enhancement based brain MRI images classification technique, Med. Hypotheses 143 (2020) 109922.
[88] F. O'Sullivan, F. Gu, Q. Wu, L.D. O'Suilleabhain, A generalized linear modeling approach to bootstrapping multi-frame PET image data, Med. Image Anal. 72 (2021) 102132.

[89] M. Reddy, P. Reddy, P. Reddy, Medical image fusion using integrated guided nonlinear anisotropic filtering with image statistics, Int. J. Intell. Eng. Syst. 13 (2020) 25–34.
[90] J.Y. Lee, J.S. Kim, T.Y. Kim, Y.S. Kim, Detection and classification of intracranial haemorrhage on CT images using a novel deep-learning algorithm, Sci. Rep. 10 (20546) (2020).
[91] D.T. Ginat, Analysis of head CT scans flagged by deep learning software for acute intracranial hemorrhage, Neuroradiology (62) (2020) 335–340.
[92] Z. Al-Ameen, Contrast enhancement of medical images using statistical methods with image processing concepts, in: 2020 6th International Engineering Conference “Sustainable Technology and Development", IEC, 2020, pp. 169–173.
[93] M. Burduja, R.T. Ionescu, N. Verga, Accurate and efficient intracranial hemorrhage detection and subtype classification in 3D CT scans with convolutional and long short-term memory neural networks, Sensors 20 (19) (2020).
[94] X. You, N. Cao, H. Lu, M. Mao, W. Wang, Denoising of MR images with rician noise using a wider neural network and noise range division, Magn. Reson. Imaging 64 (2019) 154–159.
[95] D. Prezzi, K. Owczarczyk, P. Bassett, M. Siddique, D. Breen, G. Cook, V. Goh, Adaptive statistical iterative reconstruction (ASIR) affects CT radiomics quantification in primary colorectal cancer, Eur. Radiol. 29 (2019).
[96] R.J. Miller, A. Singh, D. Dey, P. Slomka, Artificial intelligence and cardiac PET/computed, PET Clin. 17 (2022) 85–94.
[97] A.J. Bravo Valero, M.Á. Vera, Y.K. Huérfano Maldonado, Y.F. Manrique Hidalgo, A comprehensive study of a similarity criterion in cardiac computerized tomography images enhancement, Revista Facultad de Ingeniería Universidad de Antioquia (102) (2020) 51–61.
[98] M.V. Nagy, Á.L. Jermendy, F.I. Suhai, A. Panajotu, J. Csőre, S. Borzsák, D.M. Fontanini, M. Kolossváry, B. Vattay, M. Boussoussou, C.C. Novák, B. Merkely, P.M. Horvat, B. Szilveszter, Model-based adaptive filter for a dedicated cardiovascular CT scanner: Assessment of image noise, sharpness and quality, Eur. J. Radiol. 145 (2021) 110032.
[99] Y. Yahia, L. Meddeber, T. Zouagui, R. Jennane, A topology constrained geometric deformable model for medical image segmentation, Biomed. Signal Process. Control 64 (2021) 102299.
[100] F. Lareyre, C. Adam, M. Carrier, C. Dommerc, C. Mialhe, J. Raffort, A fully automated pipeline for mining abdominal aortic aneurysm using image segmentation, Sci. Rep. 9 (13750) (2019).
[101] M. Baygin, O. Yaman, P.D. Barua, S. Dogan, T. Tuncer, U.R. Acharya, Exemplar darknet19 feature generation technique for automated kidney stone detection with coronal CT images, Artif. Intell. Med. 127 (2022) 102274.
[102] S. Sudharson, T. Pratap, P. Kokil, Noise level estimation for effective blind despeckling of medical ultrasound images, Biomed. Signal Process. Control 68 (2021) 102744.
[103] R. Kaur, M. Juneja, A. Mandal, Machine learning based quantitative texture analysis of CT images for diagnosis of renal lesions, Biomed. Signal Process. Control 64 (2021) 102311.
[104] H. Akai, K. Yasaka, A. Kunimatsu, K. Ohtomo, O. Abe, S. Kiryu, Application of CT texture analysis to assess the localization of primary aldosteronism, Sci. Rep. 10 (472) (2020).
[105] A. Traverso, M. Kazmierski, Z. Shi, P. Kalendralis, M. Welch, H.D. Nissen, D. Jaffray, A. Dekker, L. Wee, Stability of radiomic features of apparent diffusion coefficient (ADC) maps for locally advanced rectal cancer in response to image pre-processing, Phys. Medica 61 (2019) 44–51.
[106] A. Bahrami, A. Karimian, H. Arabi, Comparison of different deep learning architectures for synthetic CT generation from MR images, Eur. J. Med. Phys. 90 (2021) 99–107.
[107] C. Anam, K. Adi, H. Sutanto, Z. Arifin, W.S. Budi, T. Fujibuchi, G. Dougherty, Noise reduction in CT images using a selective mean filter, J. Biomed. Phys. Eng. 10 (5) (2020) 623–634.
[108] S. Garg, R. Vijay, S. Urooj, Statistical approach to compare image denoising techniques in medical MR images, Procedia Comput. Sci. 152 (2019) 367–374, International Conference on Pervasive Computing Advances and Applications-PerCAA 2019.
[109] O. Valbuena, M.I. Vera, M. Vera, E. Gelvez-Almeida, Y. Huérfano, M. Borrero, J. Salazar-Torres, W. Salazar, Volumetric quantification in ovarian pathology using abdomino-pelvic computed tomography, J. Phys. Conf. Ser. 1403 (1) (2019) 012014.
[110] M. Vera, F. Sáenz, Y. Huérfano, E. Gelvez-Almeida, M.I. Vera, J. Salazar-Torres, O. Valbuena, Smart operator for the human liver automatic segmentation, present in medical images, J. Phys. Conf. Ser. 1386 (1) (2019) 012132.
[111] B. Prabha, S. Kaur, J. Singh, P. Nandankar, S. Kumar Jain, H. Pallathadka, Intelligent predictions of Covid disease based on lung CT images using machine learning strategy, Mater. Today: Proc. (2021).
[112] M.A. Gungor, A comparative study on wavelet denoising for high noisy CT images of COVID-19 disease, Optik 235 (2021) 166652.
[113] C.-F.J. Kuo, J. Barman, C.W. Hsieh, H.-H. Hsu, Fast fully automatic detection, classification and 3D reconstruction of pulmonary nodules in CT images by local image feature analysis, Biomed. Signal Process. Control 68 (2021) 102790.
[114] Y. Xu, L.F. Souza, I.C. Silva, A.G. Marques, F.H. Silva, V.X. Nunes, T. Han, C. Jia, V.H.C. de Albuquerque, P.P.R. Filho, A soft computing automatic based in deep learning with use of fine-tuning for pulmonary segmentation in computed tomography images, Appl. Soft Comput. 112 (2021) 107810.
[115] Z. Huang, X. Liu, R. Wang, J. Chen, P. Lu, Q. Zhang, C. Jiang, Y. Yang, X. Liu, H. Zheng, D. Liang, Z. Hu, Considering anatomical prior information for low-dose CT image enhancement using attribute-augmented wasserstein generative adversarial networks, Neurocomputing 428 (2021) 104–115.
[116] C.-F.J. Kuo, C.-C. Huang, J.-J. Siao, C.-W. Hsieh, V.Q. Huy, K.-H. Ko, H.-H. Hsu, Automatic lung nodule detection system using image processing techniques in computed tomography, Biomed. Signal Process. Control 56 (2020) 101659.
[117] Q. Liu, C. Leung, P. Hu, A two-dimensional sparse matrix profile DenseNet for COVID-19 diagnosis using chest CT images, IEEE Access 8 (2020) 213718–213728.
[118] S. Perumal, V. Thambusamy, Preprocessing by contrast enhancement techniques for medical images, Int. J. Pure Appl. Math. 118 (2018) 3681–3688.
[119] O.R. Soto, E.R. Esparza, S.E.B. Mata, D. Oliva, A.E. Hassanien, R.K. Meleppat, R.J. Zawadzki, An efficient retinal blood vessel segmentation in eye fundus images by using optimized top-hat and homomorphic filtering, Comput. Methods Programs Biomed. 201 (2021) 105949.
[120] S. Saoji, M. Sarode, Speckle and rician medical I noise removal from mages and ultrasound images, Int. J. Recent Technol. Eng. 8 (2020) 1851–1854.
[121] W. Kong, Q. Miao, R. Liu, Y. Lei, J. Cui, Q. Xie, Multimodal medical image fusion using gradient domain guided filter random walk and side window filtering in framelet domain, Inform. Sci. 585 (2022) 418–440.
[122] Y. Tang, R. Gao, S. Han, Y. Chen, D. Gao, V. Nath, C. Bermudez, M.R. Savona, S. Bao, I. Lyu, Y. Huo, B.A. Landman, Body part regression with self-supervision, IEEE Trans. Med. Imaging 40 (5) (2021) 1499–1507.
[123] M. Diwakar, P. Singh, A. Shankar, Multi-modal medical image fusion framework using co-occurrence filter and local extrema in NSST domain, Biomed. Signal Process. Control 68 (2021) 102788.
[124] U.K. Acharya, S. Kumar, Genetic algorithm based adaptive histogram equalization (GAAHE) technique for medical image enhancement, Optik 230 (2021) 166273.
[125] X. Xu, B.L. Fugen Zhou, D. Fu, X. Ba, Efficient multiple organ localization in CT image using 3D region proposal network, IEEE Trans. Med. Med. Imaging 38 (8) (2019) 1885–1898.
[126] M. Abella, C. Martínez, M. Desco, J.J. Vaquero, J.A. Fessler, Simplified statistical image reconstruction for X-ray CT with beam-hardening artifact compensation, IEEE Trans. Med. Imaging 39 (1) (2020) 111–118.
[127] T.T. Wirtti, E.O.T. Salles, A soft-threshold filtering approach for tomography reconstruction from a limited number of projections with bilateral edge preservation, Sensors 19 (10) (2019).
[128] S. Yadav, S. Kulkarni, R. Patole, Image quality assessment, denoising and comparative analysis using filters for C-arm X-ray images, in: IEEE Region 10 Conference, TENCON, 2019, pp. 2143–2147.
[129] Y. Huérfano-Maldonado, M. Mora, K. Vilches, R. Hernández-García, R. Gutiérrez, M. Vera, A comprehensive review of extreme learning machine on medical imaging, Neurocomputing 556 (2023) 126618.
[130] S. Dixon, Diagnostic Imaging Dataset Statistical Release, NHS England and NHS Improvement, 2022, Reporte, Version 1, URL https://www.england.nhs.uk/statistics/wp-content/uploads/sites/2/2022/12/Statistical-Release-15th-December-2022-PDF-487KB.pdf.

Oscar Valbuena, began his academic training by obtaining his degree in Mathematics Education at Universidad de los Andes, Táchira, Venezuela. Subsequently, he broadened his academic horizons by graduating as a Physics Specialist at the Universidad Francisco de Paula Santander, Cúcuta, Colombia, continued his academic career and obtained the degree of Magister in Mathematics Education in 2015. His passion for statistics led him to achieve the degree of Doctor in Statistics from the Universidad Central de Venezuela in 2023. Currently, he works as a researcher recognized by Minciencias at Universidad Simón Bolívar, San José de Cúcuta, Colombia, where he is a member of the Scientific Modeling and Business Innovation Research Group of the Universidad Simón Bolívar (GIMCINE), highlighting his work in the field of applied mathematics and medical image segmentation.

Vera Miguel received a degree of accreditation in mathematics education from Universidad de Los Andes, Mérida, Venezuela, in 1996. He also received M.Sc. and Ph.D. degrees in mathematics from the Universidad de Los Andes, Mérida, Venezuela, in 2005 and 2014, respectively. Currently, he is a researcher at the Universidad Simón Bolívar, San José de Cúcuta, Colombia. He is also an accredited researcher of Minciencias organization in Colombia. He is a member of the Scientific Modeling and Business Innovation Research Group of the Universidad Simón Bolívar (GIMCINE). His research interests include machine learning, mathematical modeling and segmentation of images.

Guillermo Ramírez obtained a B.Sc. degree in Statistics from the Universidad Central de Venezuela between 1969 and 1975, then a Master's degree in Statistics from the same university between 1984 and 1987, and a Ph.D. in Mathematics from the University of Salamanca between 1993 and 1995. In addition to his academic training, he has worked as Coordinator of the Postgraduate Area in Statistics at the Universidad Central de Venezuela and has contributed to research in the field of statistics and actuarial sciences.

Ricardo J. Barrientos received the B.S. degree in computer engineering from Universidad de Magallanes, Chile, the first M.Sc. degree in computer science from Universidad de Chile, Chile, and the second M.Sc. and the Ph.D. degrees in computer science from Universidad Complutense de Madrid, Spain. He is currently an Assistant Professor with Universidad Católica del Maule, Chile, and the Director of the master's program in computer science. He is also the Principal Investigator of a FONDEF project, funded by the Government of Chile, and a Researcher with the LITRP Laboratory (www.litrp.cl). His main research interests include high-performance computing and biometrics.

David Mojica, is an eighth semester student of the Systems Engineering program at Universidad Simón Bolívar, Cúcuta, Colombia. Through his commitment to systems engineering and his interest and dedication to acquire knowledge in this area of study, he is developing skills and competencies in the field of technology and computer science, collaborating significantly in the field of research.